EUROFUSION WPMAT-PR(16) 15849

J Marian et al.

Recent advances in computational materials modeling of tungsten as plasma-facing material for fusion energy applications

Preprint of Paper to be submitted for publication in Nuclear Fusion

This work has been carried out within the framework of the EUROfusion Consortium and has received funding from the Euratom research and training programme 2014-2018 under grant agreement No 633053. The views and opinions expressed herein do not necessarily reflect those of the European Commission.

Recent advances in computational materials modeling of tungsten as plasma-facing material for fusion energy applications

Jaime Marian[1], Charlotte S. Becquart[2], Christophe Domain[3], Sergei L. Dudarev[4], Mark R. Gilbert[4], Richard J. Kurtz[5], Daniel R. Mason[4], Kai Nordlund[6], Andrea E. Sand[6], Lance L. Snead[7], Tomoaki Suzudo[8], and Brian D. Wirth[9]

[1] *University of California Los Angeles, Los Angeles, CA, USA*
[2] *UMET, UMR 8207, ENSCL, U Lille, 59655 Villeneuve d'Ascq Cédex, France*
[3] *EDF-R&D, Département MMC, Les Renardières, F-77250 Moret sur Loing, France*
[4] *Culham Centre for Fusion Energy, Culham Science Centre, Abingdon, Oxon, OX14 3DB, UK*
[5] *Pacific Northwest National Laboratory, Richland WA, USA*
[6] *Department of Physics, University of Helsinki, P.O. Box 43, FI-00014 Helsinki, Finland*
[7] *Massachusetts Institute of Technology, Cambridge, MA, USA*
[8] *Japan Atomic Energy Agency, Tokai-mura, Naka-gun, Ibaraki-ken, Japan*
[9] *University of Tennessee-Knoxville, Knoxville, TN, USA*

Abstract

Under the anticipated operating conditions for demonstration magnetic fusion reactors beyond ITER, structural materials will be exposed to unprecedented conditions of irradiation, heat flux, and temperature. While such extreme environments remain inaccessible experimentally, computational modeling and simulation can provide qualitative and quantitative insights into materials response and complement the available experimental measurements with carefully validated predictions. For plasma facing components such as the first wall and the divertor, tungsten (W) has been selected as the best candidate material due to its superior high-temperature and irradiation properties. In this paper we provide a review of recent efforts in computational modeling of W both as a plasma-facing material exposed to He deposition as well as a bulk structural material subjected to fast neutron irradiation. We use a multiscale modeling approach – commonly used as the materials modeling paradigm– to define the outline of the paper and highlight recent advances using several classes of techniques and their interconnection. We highlight several of the most salient findings obtained via computational modeling and point out a number of remaining challenges and future research directions.

1 Introduction

Due to its high melting point, low erosion rates in cold scrape-off layer plasma, and small tritium retention, tungsten (W) has been selected as the material of choice in plasma facing components (PFCs), such as the divertor, for magnetic fusion devices [Zinkle and Busby (2009); Zinkle and Ghoniem (2011)]. However, the maximum allowed tungsten concentration in the core plasma is strongly restricted due to radiation losses, which requires careful measurements of divertor erosion, as well as a thorough understanding of fuel recycling and retention. PFCs are exposed to very harsh conditions due to both high-energy transient plasma discharges, known as ELMs (edge localized modes), as well as sustained heat loads and fast neutron irradiation under nominal tokamak operation.

The plasma-surface interactions (PSIs) occurring in the divertor and PFCs pose a critical scientific challenge that limits our ability to operate fusion machines by sustaining a steady-state burning plasma, along with equally challenging PSIs at the RF antennas. It is well established that PSIs constitute critically important scientific issues for fusion power, and these issues affect the PFC lifetime, as well as core fusion plasma performance and the recycling of the hydrogen fuel [Federici et al. (2001); Raffray et al. (2008); Wirth et al. (2015)]. However, currently, the best available data regarding PFC response to plasma and fusion neutron exposure comes from surrogate facilities that can only approximate real fusion conditions expected in experimental or demonstration tokamaks (known as 'DEMO') [DEMO]. It is in this context that computer simulation of materials evolution has been gaining importance as a legitimate physical tool to increase our understanding of PSI and neutron irradiation processes and complement experimental observations. Modeling and simulation have been steadily benefiting from improvements in computing capabilities, novel computational techniques for materials simulations, and advances in parallel computing algorithms. The purpose of this paper is to review the present state-of-the-art in materials simulations of W in fusion environments and highlight some of the most salient findings that modeling and simulation have produced.

Often, the simulation paradigm within which computational modeling is performed is the so-called *multiscale* approach, which relies on a parameter-passing framework in which the entire spatial and temporal domains are sub-partitioned into different regimes on the basis of the

characteristic wavelength and time frequency of the physical phenomena involved. This is the approach followed in this review, where we distinguish for simplicity from surface-centered PSI simulations and bulk-like neutron irradiation simulations. This is done with the understanding that the two phenomena may likely be linked in a synergistic way, with processes occurring on or near the surface affecting the bulk microstructural evolution, and vice versa, such as heat transport and species diffusing between these spatial domains.

Furthermore, multiscale modeling strives to provide a physically based model of materials evolution, such that information emanating from the underlying atomistic structure of materials can be elevated via parameter-passing and linking of multiple computational techniques to the macroscopic scale, where engineering response functions are measured and formulated. There are of course many grand challenges associated with this idea, whose discussion falls outside the scope of this review, but which makes computational modeling of this kind an active field of research presently. Figure 1 shows a space-time diagram showing the governing phenomena in fusion structural materials.

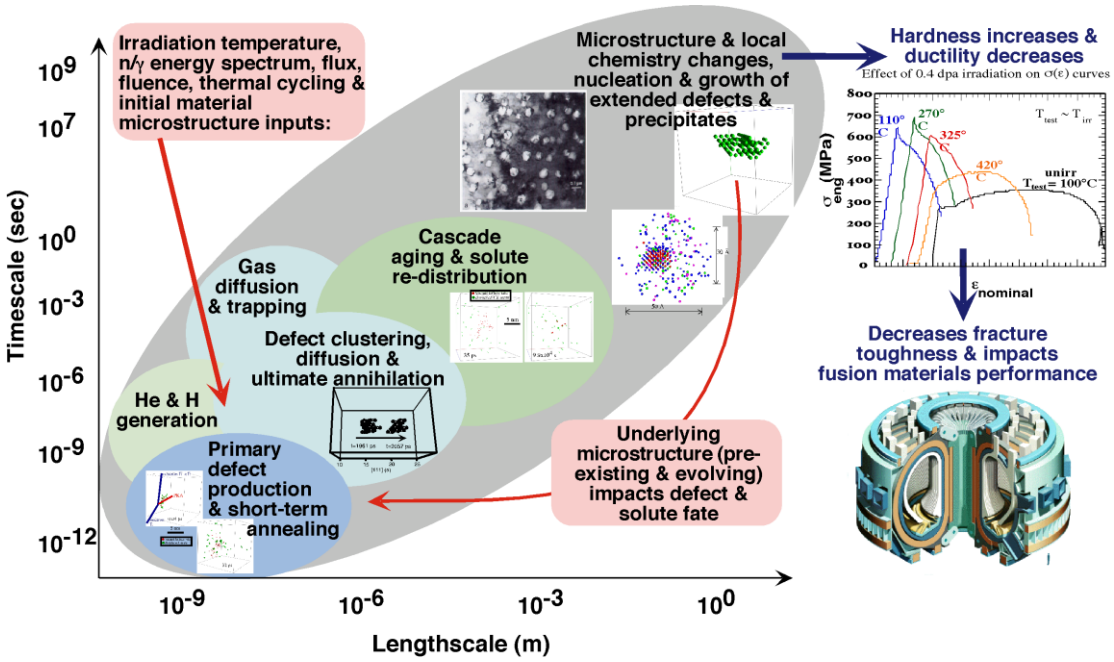

Figure 1: Schematic diagram showing the multiscale nature of microstructural evolution in fusion structural materials.

Next, we discuss recent simulations results of PSI effects in plasma-exposed W surfaces, followed by a description of the state-of-the-art in terms of bulk neutron irradiation simulations

2 Modeling plasma-surface interactions in W

Laboratory experiments performed in linear plasma devices indicate the possibility of substantial surface modification in tungsten exposed to low-energy, He plasma, or mixed He-H plasma, although the observed surface response is strongly temperature-dependent as well as on the ion energy and flux. Pitted surfaces are observed below ≈1000 K [Iwakiri et al. (2000)], whereas a "nanostructured," low-density "fuzz" or "coral" surface morphology is observed between

approximately 1000 and 2000 K [Takamura et al. (2006); Baldwin and Doerner (2008); Baldwin et al. (2009); Zenobia and Kulcinski (2009)], while micron-sized holes, or pits, are observed to form above about 2000 K [Nishijima et al. (2004); Nishijima et al. (2005)]. The nanostructured "fuzz" has also recently been observed in the divertor regions of a tokamak device operating with a He plasma [Wright et al. (2012)]. Such surface features could lead to changes in heat transfer, fuel (deuterium/tritium) retention [Baldwin et al. (2011)], increased rates of erosion through both sputtering and dust formation [Umstadter et al. (2009)], and embrittlement of the divertor, all of which can be detrimental for device operation [Hill et al. (1982)]. It is important to note that fuzz-like surface modification has not been observed for H-only plasma exposure, strongly indicating that He implantation controls this phenomenon. Transmission electron microscopy (TEM) suggests that the nanometer-scale tendrils of the fuzz, and sub-surface regions of W, contain gas bubbles and/or cavities [Kajita et al. (2007); Miyamoto et al. (2009)], which implies that bubble evolution is an important process in fuzz formation in W.

Experiments at PISCES-B [Hirooka et al. (1990); Baldwin et al. (2009)] and NAGDIS-II [Ezumi et al. (1997)] suggest that the nanostructured fuzz forms when the surface temperature is between 1000 and 2000 K for incident ion energies above 22 eV [Kajita et al. (2009)]. This raises multiple questions about the mechanisms that control surface evolution, particularly with respect to the rate of gas bubble formation as a function of temperature and gas implantation, as well as the mechanisms leading to severe surface roughening. Sharafat and co-workers (2009) suggested that near-surface stress gradients cause He bubbles to be drawn to the surface in the 1000–2400 K temperature range. Krasheninnikov (2011) has suggested a viscoelastic model of "fuzz" growth, while Kajita and coworkers (2009) indicated that "pinholes" form on the surface before the "fuzz" begins to grow and suggested that stresses created by bubble formation and growth were responsible for fuzz formation. Alternately, Marynenko and Nagel (2012) suggested that adatom formation due to sub-threshold helium impacts, combined with holes from burst bubbles, and subsequent surface diffusion, combined with the trapping (immobilization) of adatoms at the tips of growing islands/fibers are responsible for fuzz formation. Lasa and co-workers have recently used kinetic Monte Carlo simulations to investigate the growth kinetics of a porous, fuzz-like structure [Lasa et al. (2014)]. We will review some of this progress, along with progress from the atomistic to continuum scale from this multiscale paradigm, to discuss W response to low-energy He implantation in more detail below.

As low-energy He, or H isotopes, are accelerated towards a divertor or PFC surface, they can reflect, induce sputtering of surface atoms, be adsorbed onto the surface, or implanted below the surface depending on the type of ion, kinetic energy and angle of incidence. Likewise, sputtered or eroded material from a surface can be ionized, transported through the plasma and re-deposited. Since implantation energies are generally in the range of 10 to 1000 eV, the implantation depth is generally only a few nanometers. As more implanted particles accumulate within the surface layer, eventually a steady-state condition can result, in which the flux of species implanted into the material is balanced by a corresponding flux of gas species that desorb from the material. The extent to which both surface morphology and sub-surface defect creation and evolution processes driven by neutron-induced damage influence the diffusion, trapping and precipitation of hydrogen and helium species into gas bubbles is an outstanding question, which will certainly impact tritium permeation, retention and near-surface saturation levels. Figure 2 illustrates the phenomena that dictate the materials surface response to plasma exposure [Wirth et al. (2011); Wirth et al. (2015)]. Correspondingly, a wide range of computational models must be accurately integrated to describe diverse processes including the plasma boundary and scrape-off layer physics subject to electrostatic and magnetic sheaths, as well as the materials surface science. While vastly different length scales characterize the surface (~nm) and plasma processes (~mm) as indicated in Fig. 2, the plasma and the material's surface are strongly coupled to each other,

mediated by an electrostatic and magnetic sheath, through the nearly continuous exchange and recycling of incident ion and neutral species and the re-deposition of eroded particles. In this section, we exclusively focus on the materials surface response to this extreme PSI environment.

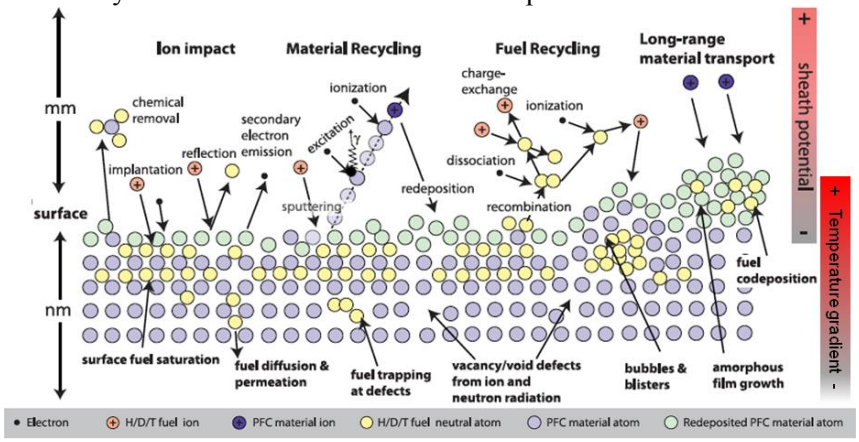

Figure 2. Schematic illustration of the synergistic plasma surface interaction processes that dictate material evolution and performance in the magnetic fusion plasma environment, as reproduced from [Wirth et al., 2011 and Wirth et al., 2015].

Multiscale modeling of PSI effects involves molecular dynamics (MD) as well as binary collision approximation, using codes such as SRIM [Ziegler (1985)] for planar surfaces, or simulations of non-planar, complex geometry surfaces with fractal features [Ruzic and Chiu (1989); Ruzic (1990)] to describe the fast (i.e., time scale < O(10 ns)) dynamic processes of sputtering, re-deposition and surface evolution, as well as bulk defect and helium/hydrogen species evolution in mixed W–He–H–Be systems. Accelerated molecular dynamics (AMD) methods [Voter (1998); Voter et al. (2002)] can be used to identify key evolution mechanisms occurring on time scales up to seconds. AMD provides a unique approach that enables deterministic simulations of plasma ion flux at appropriate rates, and captures material evolution for durations up to and beyond the time scale of seconds that are needed to identify slower, rare-event processes that contribute to surface, defect and impurity evolution. The AMD approaches, complemented by techniques for activation energy barrier identification, such as the nudged elastic band (NEB) [Henkelman et al., 2000] and the dimer [Kastner and Sherwood (2008)] method, can determine activation energies and pre-factors that are used to define, within transition-state theory, the reaction rates of individual mechanisms. First-principles density functional theory (DFT) electronic structure methods as implemented in commercial and open-source codes [Kresse and Hafner (1993); Giannozzi et al. (2009); Soler et al. (2002)] can be instrumental in providing interaction forces, basic thermodynamic and kinetic interactions and rates, which can be used in fitting interatomic potentials for molecular dynamics simulations, and will be utilized where existing interatomic potentials are deemed inadequate. Surface evolution phenomena, including re-deposition, fuzz growth and surface migration can be investigated using reduced-parameter continuum techniques [Krasheninnikov (2011)] with the goal of developing evolution models that reduce the dynamic complexity to the most pertinent and tractable variables.

Insight into mechanisms and rates of occurrence is the essential outcome of atomic-scale modeling, which can be coupled to reduced parameter models to effectively integrate across the length and time scales in a hierarchical multiscale modeling paradigm. These insights (and corresponding rates) are then used as input in a sequential (hierarchical) fashion to micron to millimeter-scale models; such coarser-scale models may be in the form of either a kinetic Monte Carlo (KMC) simulation or reaction-diffusion rate theory, or cluster dynamics approaches at the

continuum to model the long-time morphological and chemical evolution of a plasma-facing component at, near, and below the surface. In the following, we discuss several of the most salient insights obtained from computational modeling at each scale.

2.1 Molecular dynamics simulations of He exposure on W surfaces

MD is a computer simulation method for studying the dynamics of atoms and molecules. Atoms are allowed to interact for a fixed period of time giving rise to dynamic trajectories in phase space. These trajectories are determined classically by numerically solving Newton's equations of motion for a system of interacting particles, where forces between the particles and their potential energies are calculated using interatomic potentials or molecular mechanics force fields. The time resolution in MD is on the order of atomic vibrations (~fs), and calculating the atomic forces is an $O(N^2)$ problem (with N the number of particles). This limits the spatio-temporal scales directly accessible with the technique, which is nonetheless widely used in materials science and for fusion materials simulations. The key input to MD is the interatomic potential, which, for the sake of computational speed, is typically formulated semi-empirically based on input from quantum mechanical calculations and/or experimental data. In the case at hand, much effort has been devoted to developing interatomic potentials for the W-He-H-Be system and any of their pairwise variants [Björkas et al. (2010); Cusentino et al. (2015); Fang et al. (2015)]. For bulk neutron damage calculations, it is of interest to develop W-Re, W-Os, and possibly W-Pt potentials (as well as other transition metals) as a result of significant neutron induced transmutation (to be discussed later), but very little research has been directed to these systems as of yet, with efforts primarily focused on first principles calculations of defects and solute complexes in binary W alloys.

In terms of simulating fusion materials with respect to either PSI or bulk neutron damage, the main difficulty when using MD is the short time resolution, which limits simulations to accumulated times that are often less than 100 nanoseconds. For PSI simulations, the short time actually encourages researchers to implant the gas species at extremely high deposition rates that are often many orders of magnitude beyond that of today's experimental facilities. This requires a very careful approach to meaningfully extrapolate such MD simulations and/or performing validation/verifications to interpret computational results in comparison to experimental analogs at much lower rates. Numerous MD simulation studies have been conducted since the first study in 2006 to predict the response of tungsten surfaces to the implantation of He [Henriksson et al. (2006); Sefta et al. (2013); Lasa et al. (2013); Li et al. (2013); Hammond and Wirth (2014); Ito et al. (2015); Cui et al., (2015)]. In one such study, He atoms were deposited with incident ion energy of 60 eV. The He atoms were inserted below the tungsten surface without kinetic energy according to the depth profile predicted from SRIM so as to avoid dealing with morphology-preserving He reflections (70% to 90% of the total, according to experimental estimates) [Sefta et al. (2013)]. He was implanted at a rate of 2.5×10^{27} He m^{-2} s^{-1} (note that the flux expected at the ITER divertor strike point is about 10^{24} He m^{-2} s^{-1}), at 1200 K. Despite this difference, MD simulations provide practical insight into relevant mechanisms of bubble formation and growth, along with corresponding surface topology changes.

For example, MD simulations consistently reveal the following sequence of events for He implanted below W surfaces at high rate, when the He atoms have insufficient kinetic energy to sputter W or produce atomic displacements in the form of Frenkel pairs. Once the helium comes to rest below the tungsten surface, it becomes an interstitial atom within the tungsten matrix with a very high mobility. The injected He atom will thus rapidly diffuse in a more-or-less random trajectory that can result in returning to the free surface and escaping, or diffusing deeper into the solid until encountering a defect or another helium atom. Due to the essentially repulsive nature

of the He-W interactions, the He has a strong driving force to cluster (in order to minimize the number of repulsive W-He interactions). Small helium clusters are themselves mobile, as long as all of the He reside in interstitial positions in the W lattice, and any clusters that form continue to perform an essentially random walk with fast diffusivity (activation energies for interstitial helium and helium cluster migration range from about 0.15 to 0.45 eV using interatomic potentials [Perez et al. (2014)]. As the migrating helium clusters grow larger, they eventually reach a condition in which the effective pressure generated is sufficient to create a tungsten vacancy and self-interstitial (Frenkel) pair, in a process called trap mutation [Lasa et al. (2013); Sefta et al. (2013)]. The size at which trap mutation first occurs depends on a number of factors, including the temperature and the proximity of the helium cluster to the free surface, as well as the surface's crystallographic orientation [Hu et al. (2014)]. When trap mutation occurs, the high-pressure interstitial helium cluster situates itself on or near the newly created vacancy, and the cluster essentially becomes immobile since it now requires either additional vacancies or interstitial-vacancy recombination and kick-out mechanisms to diffuse. A helium-vacancy cluster containing multiple helium atoms then serves as a nucleus for growing helium gas bubbles at higher fluence, through the absorption of mobile helium interstitial atoms and helium clusters during continued gas implantation. As the high-pressure gas bubbles continue to grow and the pressure in the bubbles continues to rise due to the absorption of additional helium, eventually this pressure reaches the level required for dislocation loop punching [Henriksson et al. (2006); Ito et al. (2014); Lasa et al. (2013); Sefta et al. (2013); Sandoval et al. (2015); Smirnov et al. (2015)]. The punching of prismatic dislocation loops allows the volume of the gas bubbles to increase through absorbing a prismatic platelet or facet of vacant lattice sites and thereby reducing their pressure. The fate of the tungsten interstitial atoms produced by either trap mutation or dislocation loop punching is strongly influenced by the presence of a nearby free surface, where image forces attract the dislocation loop to the surface, leading to significant roughening of the tungsten surface through the formation of individual W adatoms as single self-interstitials annihilate at the surface, and formation of coherent islands of tungsten atoms formed by way of annihilation of prismatic loops. The final process observed in MD simulations is the rupture of over-pressurized He gas bubbles located near the surface [Henriksson et al. (2006); Lasa et al. (2013); Sefta et al. (2013); Sandoval et al. (2015)].

Figure 3 shows a bubble rupture event from such MD simulations following He accumulation in subsurface bubbles that grow via interstitial loop punching [Sefta et al. (2013)]. Simulations that include microstructural features such as grain boundaries (right figure) have also been carried out to assess the importance of trapping sites in W surfaces. These MD simulations result in surface morphology evolution by the combined effect of He kinetics coupled to loop punching and surface inhomogeneities. Figure 4 shows a snapshot correlating the sub-surface He concentration in tungsten to the surface morphology, following slightly over 1 micro-second of MD simulation at a high rate of ~10^{27} He $m^{-2}s^{-1}$, using a 100 eV He implantation energy at 933 K [Hammond et al. (2016)]. In a very recent work combining experiments and MD simulations of 300 eV Helium implantation process into W at 300 K, Pentecoste et al. (2016) have shown that He diffusion, formation and coalescence of clusters are the phenomena leading to the flaking of the substrate and that these processes could explain the saturation of the retention observed experimentally at low energies.

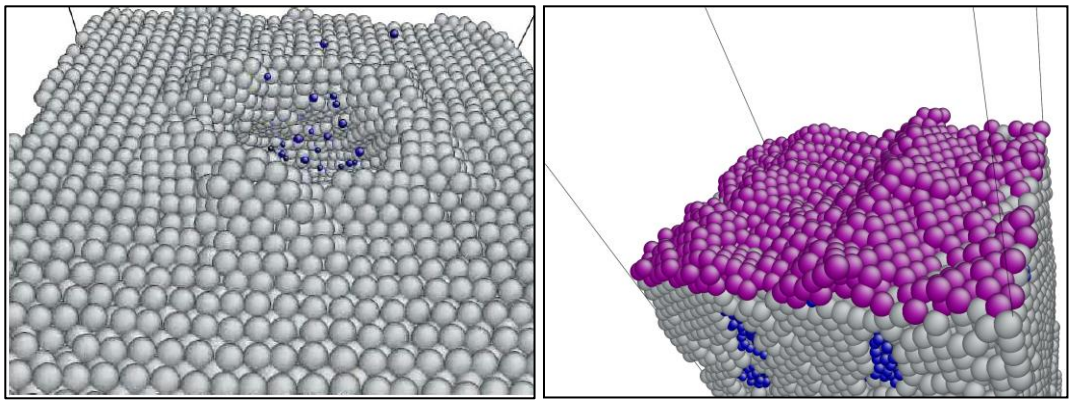

Figure 3: Atomistic views of a He-bubble rupture event (left) and rapid surface topology evolution in the form of 'ridging' produced by He accumulation at a grain boundary (right), in which gray spheres denote tungsten atoms, magenta are tungsten adatoms produced as self-interstitial atoms or pristmatic dislocation loops annihilate on the free surface, and blue spheres are helium atoms.

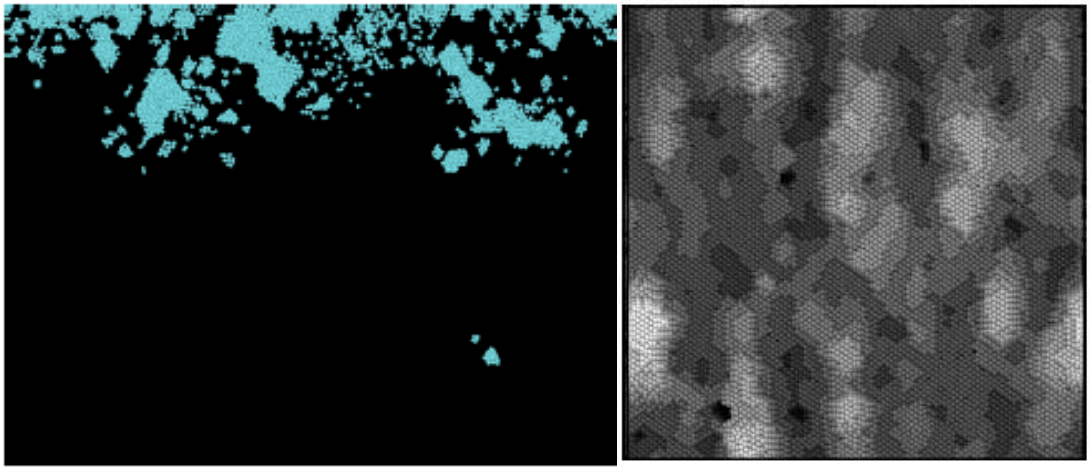

Figure 4: Snapshots from an MD simulation of (110) tungsten surface response at 933 K to 100 eV helium implantation at a flux of 5.5×10^{26} $m^{-2}s^{-1}$ to a fluence of 6.6×10^{20} m^{-2}. The left image shows a cross-section view of the sub-surface helium bubble population (light blue circles represent individual helium atoms) in The right image is a top-down perspective of the surface topology evolution, in which individual tungsten atoms are imaged as colored spheres, in which a linear grayscale has been imposed with black spheres being 0.5 nm below the original (110) surface, and white spheres are +2 nm above the original surface [Hammond et al. (2016)].

It is worth mentioning that other researchers have obtained qualitatively similar results doing independent MD simulations [Lasa et al. (2013); Li et al. (2013); Ito et al. (2015)], which provides consistency checks for the atomistic mechanisms briefly described here.

2.2 Kinetic Monte Carlo simulations

Kinetic Monte Carlo (KMC) is used to simulate the long-time dynamics of this many-body system evolving through a sequence of states connected by diffusion events. The method is formulated on the basis of Markovian (random) walks, such that each state transition is independent of the previous one, and the time increment behaves as a Poisson variate [Fichthorn and Weinberg (1991); Voter (2005)]. The main advantage of KMC is that, rather than following the trajectory of the system through every vibrational period (fs), these state-to-state transitions are treated directly, which can result in time scale gains of several orders of magnitude. The

physical fidelity of KMC hinges on the set of physical events included and the accuracy of the transition rates, which represent the probability per unit time that a system will suffer a transition between two different states (also known as an 'event'). Transition rates typically depend on energy barriers that separate the two states, which must be calculated using atomistic methods in what is by now a fairly well-established procedure [Voter (2005)]. For radiation damage simulations, there are several variants of KMC depending on the level of accuracy and the application:

- Lattice KMC (LKMC) is carried out on a fixed lattice described by an integer coordinate system. Otherwise it is called off-lattice KMC.
- Atomistic KMC (AKMC), where the diffusing entity is an atom or clusters of atoms.
- Object KMC (OKMC): Usually the diffusing entities are point defects and their clusters that are jumping either in random or lattice-specific directions. Only the positions of the jumping objects are included in the simulation, not those of the "background" lattice atoms. The basic KMC step is one object jump.
- Event KMC (EKMC) or First-Passage KMC (FPKMC): Denotes an OKMC or AKMC simulation where reactions or interactions between objects (e.g. clustering of two impurities or vacancy-interstitial annihilation) are chosen by the KMC algorithm, taking object positions into account, and the event is then immediately carried out [Dalla Torre et al. (2005); Oppelstrup et al. (2005)].

An interesting application of kinetic Monte Carlo to fusion PSI issues is the formation of fuzz in He-exposed W has been carried out by researchers at the University of Helsinki, who performed OKMC simulations under experimental conditions and found that surface roughness, akin to formation of a fuzz layer, increases in thickness with a square root of time dependence, consistent with experimentally measured fuzz thickness [Lasa et al. (2014)]. These workers rationalized the square root dependence of the fuzz layer growth in terms of a two-step mechanism composed of subsurface He-bubble nucleation and growth, bubble rupture due to directional growth by interstitial loop emission, and surface roughness formation. It is interesting to note that these OKMC simulations did not include any lattice stress or viscoelastic effects, nor any W surface diffusion or W knock-out adatom formation, and yet they predict a $\sqrt{t}$ dependence, suggesting that these mechanisms may not be critical to explain the fuzz growth behavior. Figure 5 shows the growth of the fuzz layer thickness as a function of time comparing experimental results with OKMC calculations.

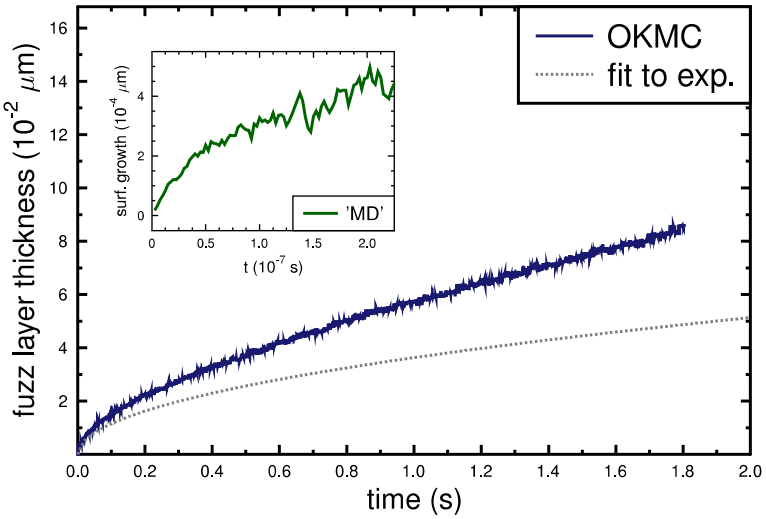

Figure 5. The fuzz layer thickness as a function of time comparing experimental results with OKMC calculations. Inset: the surface growth obtained in direct MD cells as a function of time. From Lasa et al. (2014).

Irrespective of whether these simulations represent a full explanation to the observed fuzz growth behavior, they undoubtedly showcase the capabilities of KMC simulations in terms of capturing the relevant physical phenomena and approaching experimentally-relevant timescales.

2.3 Connecting atomistic information with continuum kinetic models

Reaching timescales (or, equivalently, irradiation/implantation doses) of relevance for surface and microstructural evolution requires approximations to reduce the number of degrees of freedom involved and boost the computational efficiency several fold. The most popular homogenization approach is the so-called mean field approximation, in which the interactions of a many-body system are replaced with an average or effective interaction. This reduces any multi-body problem into an effective one-body problem, resulting in significant computational gains at the expense of neglecting spatial correlations and stochastic fluctuations. In the context of defect population evolution, mean field rate theory (MFRT) provides solutions to a Master Equation (ME) that describes both growth and dissolution of the clusters due to reactions with mobile defects (or solutes), thermal emission of these same species, and cluster coalescence if the clusters are mobile. The relevant physical processes require accounting for clusters containing a very large number of point defects or atoms ($>10^6$), particularly for high irradiation doses or long ageing times. Discretization of the ME in terms of the cluster species leads to a system of coupled ordinary differential equations (ODE) in which time is an explicit variable. The number of equations is the same as the number of cluster species (and/or solutes) in the largest possible cluster. Numerical integration of such a system is feasible on modern computers, although practicable solutions to the ME still make use of grouping procedure to significantly reduce the number of equations [Stoller et al. (2008)].

One added feature of MFRT required for PSI simulations is the need for spatial resolution in order to resolve depth effects and He subsurface accumulation. This has resulted in the development of MFRT codes such as *Xolotl* [Xolotl], which is a parallel code used to solve advection/reaction/diffusion cluster dynamics problems within spatially-resolved continuum domain in 2D or 3D. These codes consider a continuum concentration of He, vacancies, interstitials and mixed clusters at spatial grid points, solving the coupled advection-reaction-diffusion equations. Figure 6 shows a schematic picture of the atomistic morphology of an evolving PFC surface and its equivalent discrete 2D representation for MFRT calculations.

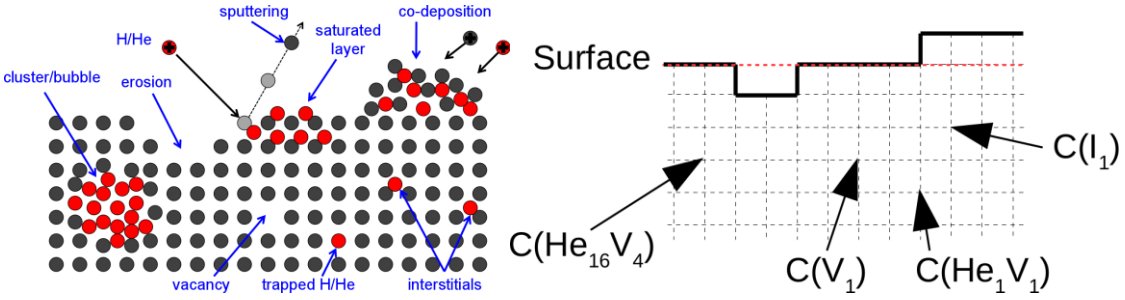

Figure 6: Schematic atomistic representation of a W-He surface (right) and its equivalent representation in terms of a spatially discretized mesh for MFRT calculations.

An example of hierarchical modeling starting with atomistic calculations leading into a parameterized cluster dynamics model was conducted by Maroudas et al (2016). These authors

studied the problem of helium segregation on surfaces of plasma-exposed W using a parameter-passing approach initiated with MD simulations. The simulations employ carefully parameterized interatomic interaction potentials which are then used to calculate the energetics of He surface segregation. Targeted large-scale MD simulations can then provide information about near-surface He cluster reactions and their evolution in plasma-exposed tungsten. For example, these MD simulations have shown that the clusters' drift toward the surface enables cluster reactions, such as trap mutation, in the near-surface region at rates much higher than those of the corresponding reactions in the bulk material. This near-surface cluster dynamics have significant effects on the surface morphology, near-surface defect structures, and the amount of He retained in the material upon plasma exposure. This information is then integrated into a properly parameterized continuum-scale cluster transport-reaction dynamics model, which can be cross-verified by comparing its predictions with those of the large-scale MD simulations on shorter time scales. Figure 7 shows the cumulative helium distributions, as a function of surface orientation, obtained from MD compared to the continuum cluster-dynamics model.

The cluster-dynamics model, which was implemented computationally through *Xolotl*, is a fully atomistically informed coarse-grained model that sets the stage for computationally efficient simulation predictions of He surface segregation, He retention, and surface morphological evolution toward optimal design of plasma facing components. The physics of He segregation, cluster transport, and cluster reactions in the bulk and near the surface are incorporated into the cluster-dynamics modeling framework. Extending this framework to include helium bubble physics, away from the dilute limit of helium concentration, and their impact on surface morphology and near-surface structure is currently under way and will be reported in forthcoming publications.

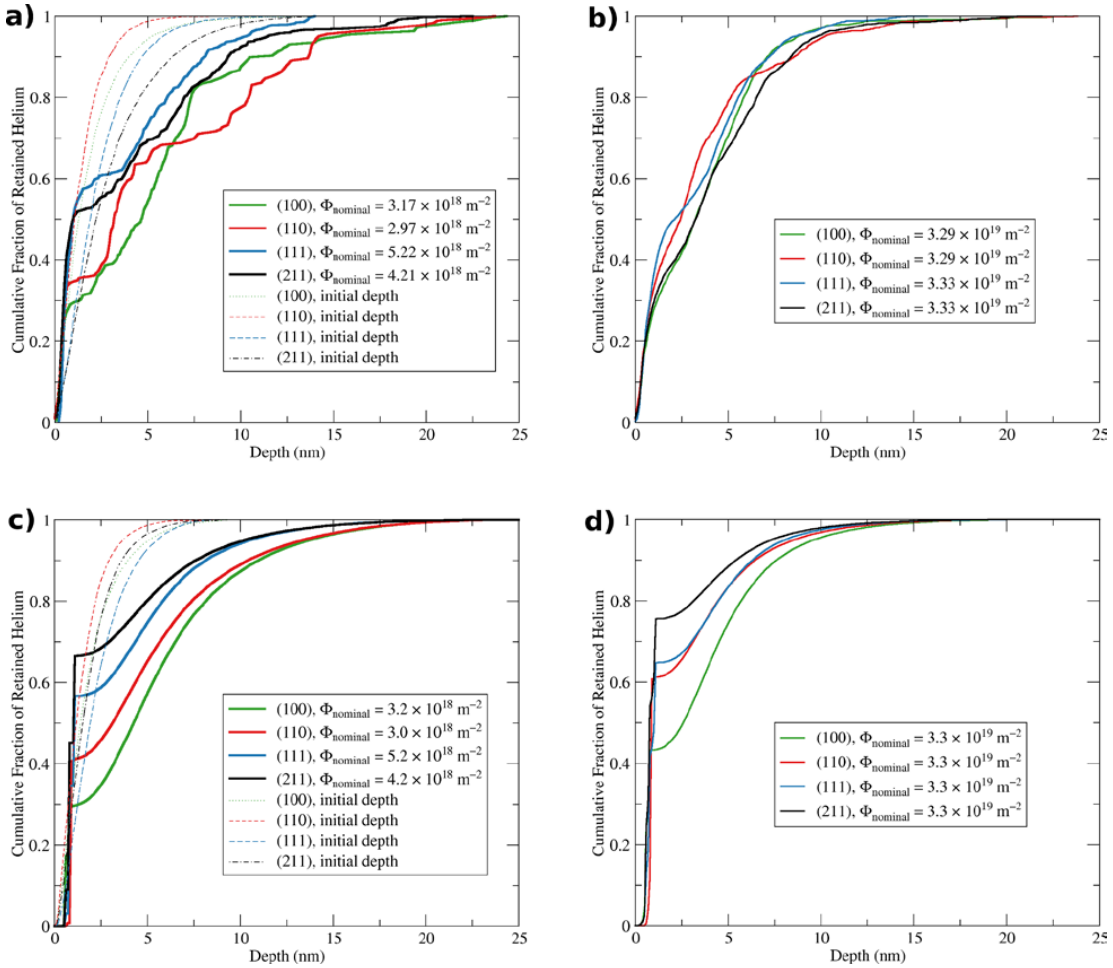

Figure 7: Cumulative helium distributions, as a function of surface orientation, obtained from MD (a and b) and the continuum cluster-dynamics model (c and d), at a nominal flux of 4.0×10^{25} He $m^{-2}s^{-1}$ and a fluence of 3.3×10^{18} He m^{-2} (a and c) versus a fluence of 3.3×10^{19} He m^{-2} (b and d).

3 Bulk effects in neutron irradiated W

Unfortunately, while the effects of irradiation in W have been studied for decades, starting from pioneering investigations of resistivity recovery stages in neutron-irradiated tungsten by Thompson (1960), and swelling in neutron-irradiated tungsten by Matolich et al. (1974), due to the variability in the quality of the tungsten materials studied, our fundamental understanding is still limited. As with many refractory metals, W mechanical properties are strongly dependent on the internal microstructure, with the grain boundaries profoundly influenced by the fabrication route and post-fabrication thermo-mechanical processing. This, and the presence of alloying elements, has a strong effect on irradiation-induced embrittlement of tungsten, a phenomenon that imposes constrains on the use of tungsten as plasma-facing material in fusion devices [Bolt et al. (2002)]. The most common form of W metal used in the majority of irradiation studies is sintered tungsten, whose intrinsically brittle behavior becomes rapidly more pronounced following irradiation. However, this is more likely due to a weakening of the grain boundaries due to processing, rather than an intrinsic issue of the W crystal. The main source of information

regarding the behavior of single crystal and very pure W under neutron irradiation comes from a series of independent experiments performed at the JOYO fast reactor in Japan [Tanno et al. (2009); Hasegawa et al. (2011)] and at the HFIR mixed spectrum reactor at the Oak Ridge National Laboratory [Snead et al. (2013)]. Notwithstanding differences in neutron spectra and irradiation dose, both sets of experiments agree on the qualitative response of irradiated W crystals, characterized by a sequence of microstructural transformations with increasing irradiation dose. In the temperature range studied of 400~800°C, these range from (i) the formation of dislocation loops, (ii) the onset of a void lattice, (iii) the dissolution of the void lattice and the emergence of small lenticular Re/Os precipitates, followed by (iv) phase separation of transmutation species into needle-shaped precipitates. During this process substantial hardening occurs both due to sessile defect creation and due to slow build-in of transmutation intermetallics. Figure 8 shows the transformation sequence schematically for the doses recorded at JOYO by Hasegawa and co-workers between 400 and 800°C [Hasegawa et al. (2013)].

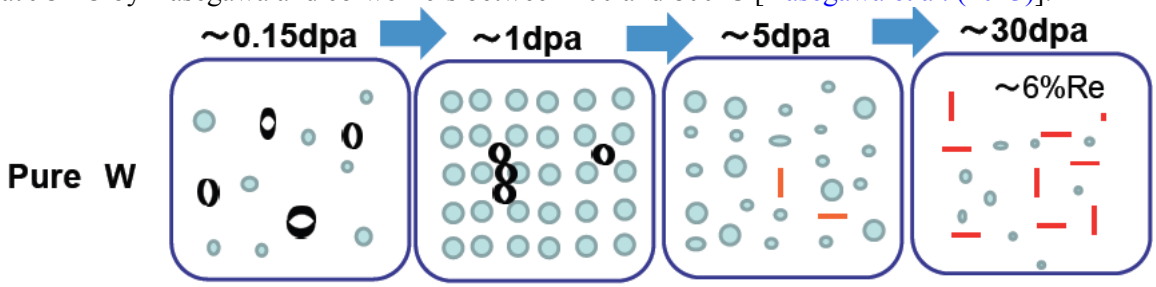

Figure 8: Schematic microstructural evolution sequence for fast neutron irradiation of W. Circles represent voids, black loops represent interstitial dislocation loops, red sticks represent elongated Re-rich precipitates.

Irradiation experiments at ORNL have confirmed Hasegawa's group's results and have extended the range of microstructural transformations to lower temperatures and longer irradiation doses. A schematic microstructural map of the irradiation microstructure, as first proposed by JOYO group and extended by ORNL researchers, is provided in Figure 9.

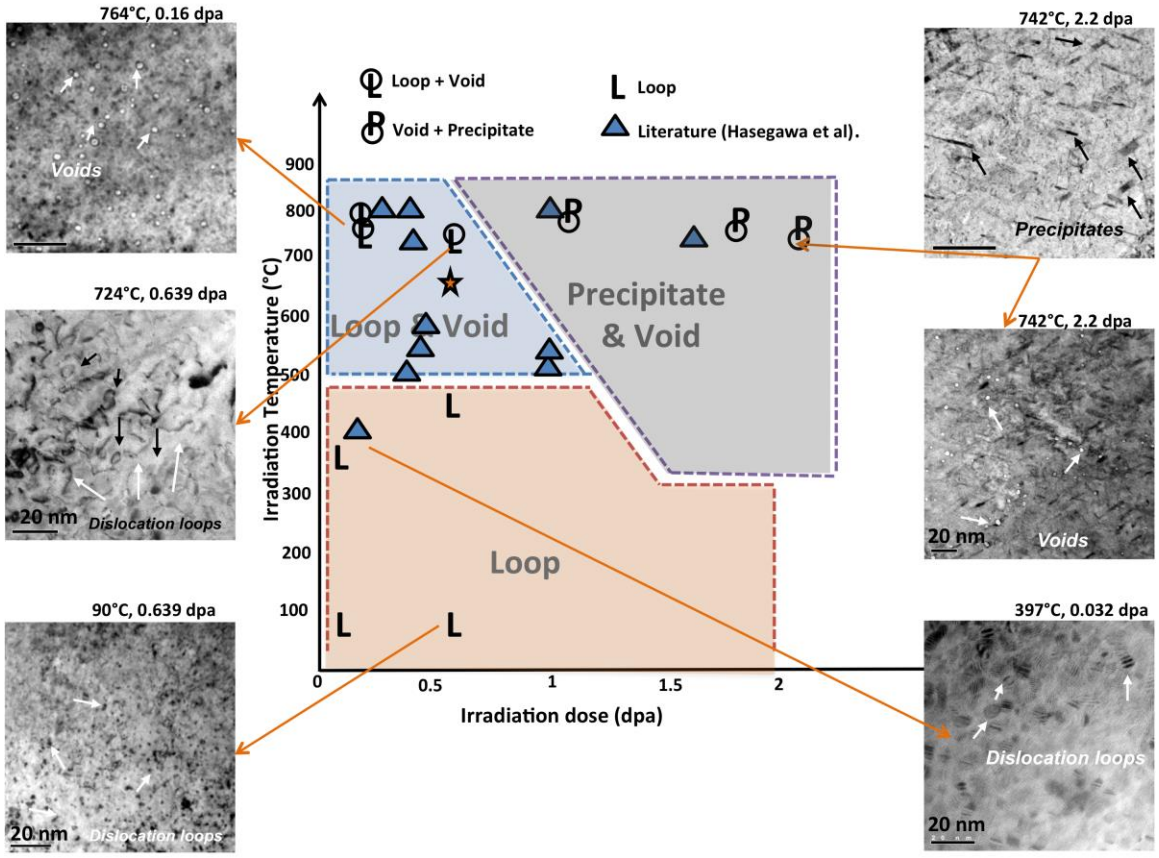

Figure 9: Irradiation phase diagram corresponding to neutron irradiated W in HFIR [Snead et al. (2016)].

The accumulation of defects of different classes depending on temperature and neutron dose is always accompanied by drastic increases in hardness and loss of ductility, which compounds unirradiated W's already low fracture toughness. The relative amount of hardening attributable to cascade-induced defects as compared to transmutation-produced intermetallics is a rather weak function of the irradiation temperature below 1000°C and a stronger function of neutron spectrum, though the relative contributions have yet to be completely sorted. However, the hardening is substantial and occurs at a relatively low dose, as seen in Figure 10. Clearly from the figure, rather than approaching a typical saturation hardening, tungsten appears to continue aggressive hardening while the tensile strength and ductility significantly degrade. In addition to these findings, several puzzling observations are made, chief among which is the precipitation of transmutation phases at concentrations well below the solubility limit. The coexistence of different kinds of irradiation defects together plus transmutation species and complex microstructures, all displaying strongly correlated behavior and synergism, results in extreme modeling challenges. The logical modeling approach to deal with these is to simulate the sequence of microstructural transformations observed piecemeal, by subdividing the observed behavior into a coherent set of phenomena again linked together by a parameter passing, multiscale framework. This is the subject of the next section.

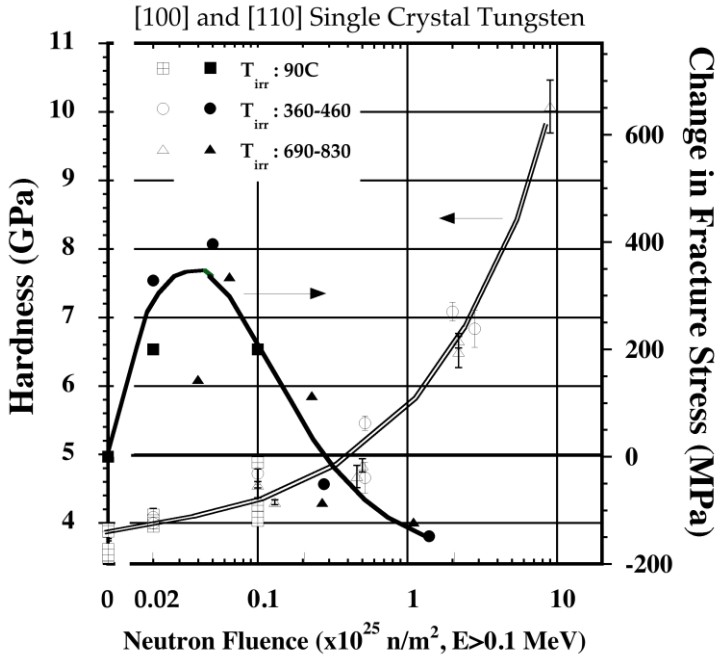

Figure 10: Increase in Vicker's hardness and change in tensile fracture stress for HFIR neutron irradiated single crystal tungsten. Hardness measured at ambient temperature. Tensile fracture stress measured near irradiation temperature [Snead (2016)].

4 Multiscale modeling of bulk neutron damage in single crystal W

4.1 Physical insight from transmutation calculations

Calculations of transmutation rates, computed via suitable inventory codes using the latest nuclear reaction data libraries, can provide valuable predictions of composition changes, radioactivity, gas production, damage rates, and more, induced in a material exposed to the high neutron fluxes expected in future fusion power plants. In particular, information about the time-evolution in chemical composition, including gas production, is an important starting point when predicting changes in mechanical, structural, and thermodynamic behavior of irradiated reactor components. For example, Figure 11 depicts a time sequence of composition snapshots for pure W under the neutron irradiation environment predicted for the outboard equatorial first wall of a conceptual design for DEMO – specifically one based around a He-cooled pebble-bed breeder blanket (cf. Pereslavtsev et al. (2014), and Figure 1 in Gilbert et al. (2015)) for more details). The evolution in composition was calculated using the FISPACT-II inventory code [Sublet et al. (2015)] with the TENDL-2014 [Koning et al. (2014)] nuclear data libraries. The composition at a particular time is presented in a 'chart of the nuclides' [Gilbert et al. (2014)] tableau, with the concentration of each nuclide in the system given using a color scale. Beginning with the initial composition of pure W at t=0, showing the concentration of the five natural occurring isotopes, the figure shows how a large number of additional isotopes are created under neutron irradiation, and also how their concentration changes (increases or decreases) with time. In particular, the newly created isotopes can belong to entirely different elements to those in the input composition, which for W means isotopes of Re, Os, Ta, etc. The smaller plot in each snapshot shows additionally the production of He and H gas. Helium gas, in particular, can lead to grain-boundary

embrittlement [Gilbert et al. (2012)], especially when complemented by direct He implantation from the fusion plasma, as has been observed experimentally by Gerasimenko et al. (1998). Obviously, this change in chemical composition must be taken into account when formulating higher-level damage models of microstructural evolution. In W, in particular, the relatively high transmutation rates (compared to other important fusion materials such as steels) to Re and Os demonstrated by these calculations and also seen experimentally [Noda et al. (1998)] is a particular concern because they have a tendency to form sigma-phase precipitates, leading to embrittlement and hardening [Nemoto et al. (2000)]. However, such changes in composition can also be beneficial; for example, Re has been observed to reduce swelling in W under high-dose irradiation [Smid et al. (1998)].

The isotopic inventory, such as that presented in Figure 11, should guide subsequent calculations of defect (and solute) species to inform damage accumulation codes. In particular, due to the computational cost of DFT calculations of defect and solute energetics, modelers should discriminate among all species potentially identified during the transmutation analysis and select the more relevant ones. Some of the most salient DFT calculations are discussed next.

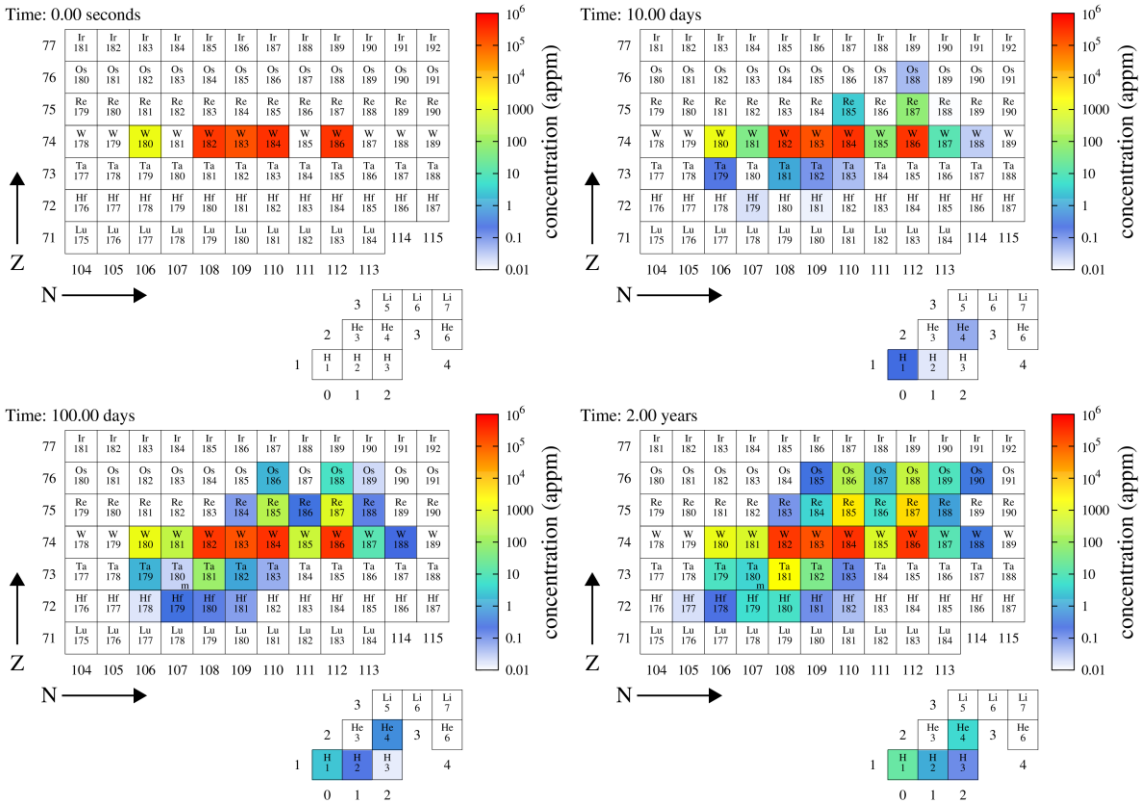

Figure 11: Sequence of nuclide concentration maps showing the time evolution of composition of initially pure W during a 2 full-power-year irradiation under the conditions predicted in the first wall of a DEMOnstration fusion power plant. The irradiation time associated with each compositional snapshot is shown in the top-lefthand corner of each map. An *m* in the box of a nuclide indicates that its concentration comes primarily from one of its *m*etastable states rather than the ground state.

4.2 DFT calculations

A substantial fraction of present-day electronic structure calculations, covering such a variety of topics as magnetic materials, vacancies and impurities, quasi-crystals, surfaces, clusters and biomolecules, relies on the pseudopotential (PP) framework. The PP approach is based on the

observation that most physical and chemical properties of atoms are determined by the structure and dynamics of the atomic valence states. This is true in particular for the formation of chemical bonds, but also for the magnetic behavior and for low-energy excitations. On the other hand, these properties are affected only indirectly by the electrons filling the deeper-lying levels, the so-called *core electrons*. The main reason for the limited role of the core electrons in many processes is the spatial separation of the core and valence shells which originates from the comparatively strong binding of the core electrons to the nucleus [Vanderbilt (1990)].

The use of PPs has simplified tremendously the complexity of DFT calculations, and all calculations discussed here have been obtained within the PP framework. Typically, supercells containing a few hundred atoms can be simulated relatively expediently. Clearly, however, this system size only allows studying point defects or very simple defect and/or solute configurations. The calculations presented here were performed in 128, 250 atom supercells with 8 *k*-points (the number of grid points in the Brillouin zone). All the structures are then relaxed by conjugate gradient, keeping the volume constant. The uncertainty in the *ab initio* results, according to years of experience with these calculations, is close to 0.01 eV for the data presented in this paper. Note that different approximations or the use of different pseudo potentials are likely to produce results that differ by more than 0.01 eV from these.

4.2.1 Point defects in pure W

Regarding point defect properties, the stability of point defect clusters has been investigated by several authors. The formation (~3.6 eV) and migration (~1.8 eV) energies of vacancies in pure tungsten derived from *ab initio* simulations are in good agreement with experimental observations [Balluffi (1978)]. A di-vacancy is unstable, and interaction between two vacancies is strongly repulsive when the two vacancies are second nearest neighbours [Becquart et al. (2007); Ventelon et al. (2012)], however it can be stabilized by solute atoms, for instance C or He atoms [Becquart et al. (2010); DeBacker et al. (2012)]. Furthermore, small vacancy clusters become stable when they contain more than three vacancies [Becquart et al. (2007); Muzyk et al. (2011)]. The most stable configuration for the self-interstitial atom is the <111> dumbbell [Nguyen-Manh et al. (2006); Derlet et al. (2007); Becquart et al. (2007)]. SIA clusters are very stable [Becquart et al. (2010); Boisse et al. (2014)] and represent nano-scale precursors for prismatic dislocation loops [Gilbert et al. (2008)]. SIA defects and SIA clusters in tungsten are highly mobile, as confirmed by experimental observations by Amino et al. (2011). The interaction of solute atoms with inert gas atoms [Nguyen-Manh et al. (2015)] and possible impurities in the W matrix has also been investigated [Becquart et al. (2010); Liu et al. (2011)]: C binds very strongly with both the vacancy and the SIA, and so does H. The binding energy of an SIA with H is not negligible: 0.20 eV, and the binding energy of a vacancy with H is high: 1.43 eV [Heinola et al. (2010)], In a previous work, it was shown that H binds also very strongly with He clusters [Becquart et al. (2009)], in agreement with the experimental findings that He pre-irradiation of metals efficiently enhances the retention of hydrogen isotopes in the penetrated region. Mo does not appear to establish any interactions with vacancies, contrarily to Re whose binding energy with the vacancy is around 0.2 eV. Mo and Re strongly interact with the SIAs (as will be shown below). The binding energy of He and the vacancy is very high, close to 4.5 eV [Becquart et al. (2007)]. This strong binding energy is the reason why the formation of nanovoids can be observed in the track region of He implanted tungsten, i.e. in a region where only a very small amount of He is implanted [DeBacker et al. (2012)]. These last results were obtained by combining DFT results in the Object Kinetic Monte Carlo LAKIMOCA [Domain et al. (2004)]. LAKIMOCA is a lattice based OKMC developed initially for Fe alloys (ferritic and austenitic). Impurities such as residual Mo atoms are treated as immobile traps, whereas foreign interstitial atoms such as C, He

or H are mobile species that can interact with point defect and point defect clusters. OKMC will be described in a later paragraph in the context of a code very similar to LAKIMOCA. Extended defects such as grain boundaries and dislocations have also been studied both due to their possible trapping capabilities and as potential short paths for diffusion. The interaction energy of H atoms with a screw dislocation ranges between 0.35 to 0.55 eV depending on the amount of H already in the dislocation [Terentyev et al. (2014)], while interaction energies with dislocation jogs and dislocations loops range between 1.2 [Terentyev et al. (2014)] and 1.76 eV [Xiao et al. (2012)]. The binding energy of H with grain boundaries varies between 0.8 and 1.5 eV depending on the grain boundary orientation and the amount of empty sites or vacancies in the grain boundary [Xiao et al. 2012, Zhou et al. (2010)].

As was discussed in Section 2.1, helium is also attracted to grain boundaries [Zhou et al. (2009)] and prefers to occupy larger spaces. Recent OKMC simulations parameterized with DFT calculations suggest that nanocrystalline W might display a higher resistance to irradiation than single crystal tungsten because He bubbles inside the nanograins are less pressurized [Martin-Bragado et al. (2013)], a fact that can be inferred from recent He irradiation experiments [Valles et al (2014)].

4.2.2 Clustering behaviour of He and H:

DFT calculations indicate that H in a W vacancy occupies a site displaced slightly towards an octahedral site, whereas He occupies the centre of the vacancy [Becquart et al. (2009)]. Regarding the formation of foreign interstitial atom clusters, it was found that in W, the H-H states are unstable for small interatomic distances whereas He-He states are strongly bound. DFT investigation of this effect in W [Becquart et al. (2009)] indicates that the He-He interaction is purely elastic in nature and, as such, highly binding at close separation distances whereas the H-H interaction is almost negligible since the elastic binding effect is compensated for by the change in effective position of the H states in the electronic structure. If the H ions are at short separation distances, the bonding and anti-bonding states are asymmetrically shifted upwards in energy, thus raising the interaction energy to result in a weak repulsion instead of the weak attraction suggested by a pure elastic analysis. The asymmetric split depends on distance in the same manner as the elastic interaction does. As a result the formation of H blisters in W can only take place in the vicinity of a defect or a solute atom, whereas He can form stable clusters in an otherwise perfect matrix. This latter point added to the fact that He moves very fast in the W lattice [Becquart et al. (2006)], which explains the strong tendency for He to form He clusters and bubbles. A recent review of data regarding the behavior of H in W was published by Lu et al. (2014). As mentioned above, H cannot form stable clusters unless it is trapped by a vacancy, or a regions with extra open volume, such as at a grain boundary, which seems to be the most effective trapping site for H, capable of accommodating up to 12 H atoms [Ohsawa et al. (2010); You et al. (2013); Fernandez et al. (2015)].

The binding energies in W of selected impurities with He and small He clusters have been determined by Becquart et al. (2011). In agreement with van der Kolk et al. [Van der Kolk et al. (1985)], most of the substitutional impurities investigated can trap He atoms as well as small He clusters. The exception is Re, and it is thus anticipated that the introduction of Re, either to improve the mechanical properties or because of transmutation will not affect He transport in W. Unlike Kornelsen (1972), it is found that both C and O are also capable of trapping He atoms. The data in Figure 12 clearly show the influence of the solute size, as the interaction of 3*d* transition metals (TM) solute is always larger than for the larger 4*d* and 5*d* TM solutes which are closer in size and binding energy with He atoms. Furthermore, we find that in general early transition metals bind with He atoms less than late ones.

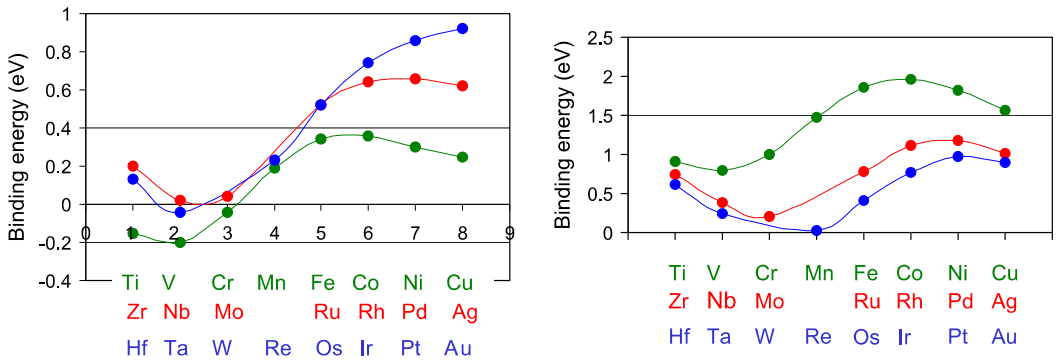

Figure 12: First nearest-neighbor binding energies (eV) between (left) solute atoms and a vacancy and (right) substitutional transition metals solute atoms and He in W predicted by DFT. The calculations were performed using the VASP code, in the PAW approach and 128 atom supercells. All the solute elements were found to be nonmagnetic.

4.2.3 He-defect complexes in W

Density functional theory calculations and molecular dynamics with a recently developed potential for W-He [Juslin et al. (2013)] were used to evaluate the thermal stability of He-vacancy clusters (*n*He-*m*V) as well as pure interstitial helium clusters in tungsten [Boisse et al. (2014a; 2014b)]. The stability of such objects results from a competitive process between thermal emission of vacancies, self-interstitial atoms (SIAs) and He atoms, depending on the He-to-vacancy ratio in mixed clusters or He number in pure interstitial He clusters. Becquart et al. (2007) have investigated in particular the ground state configurations as well as the activation barriers of self-trapping and trap mutation, i.e. the emission of one SIA along with the creation of one vacancy from a He-V or pure He object. A clear dependence of the binding energies of *n*He-*m*V clusters with the *n*/*m* ratio has been observed and can be viewed as an effect of the He density, that is, the pressure inside the bubble. However, the larger the *n*He-*m*V cluster the more favorable the SIA emission process. Calculations show that the emitted SIA is bound to the *n*He-*m*V clusters and even more strongly bound when a SIA is already trapped. The dynamics of the self-trapping has been investigated using MD simulations. Self-trapping is thermally activated and Arrhenius plots of the process by MD give activation energies that have been compared to the ones obtained by NEB calculations. They are found to be around 0.5 eV for 7He clusters or 8He clusters by the dynamic method and between 0.5 and 0.9 eV by the NEB. It has been shown that the dissociation model which is often used to calculate activation energy cannot be applied to self-trapping and trap mutation. A sensible extrapolation of the self-trapping activation energy has been proposed for the self-trapping of He clusters containing up to 12He which clearly suggests that the energy barrier for Frenkel Pair recombination increases with the cluster size. All these data have been introduced in the OKMC code LAKIMOCA to model self trapping and trap mutation. In any case, the energetics of *n*He-*m*V clusters is essential to describe the long-term stability of He bubbles in continuum models. This constitutes the so-called equation of state for pressurized He bubbles, shown in Figure 13 as calculated with DFT methods in by Boisse et al. (2014a; 2014b).

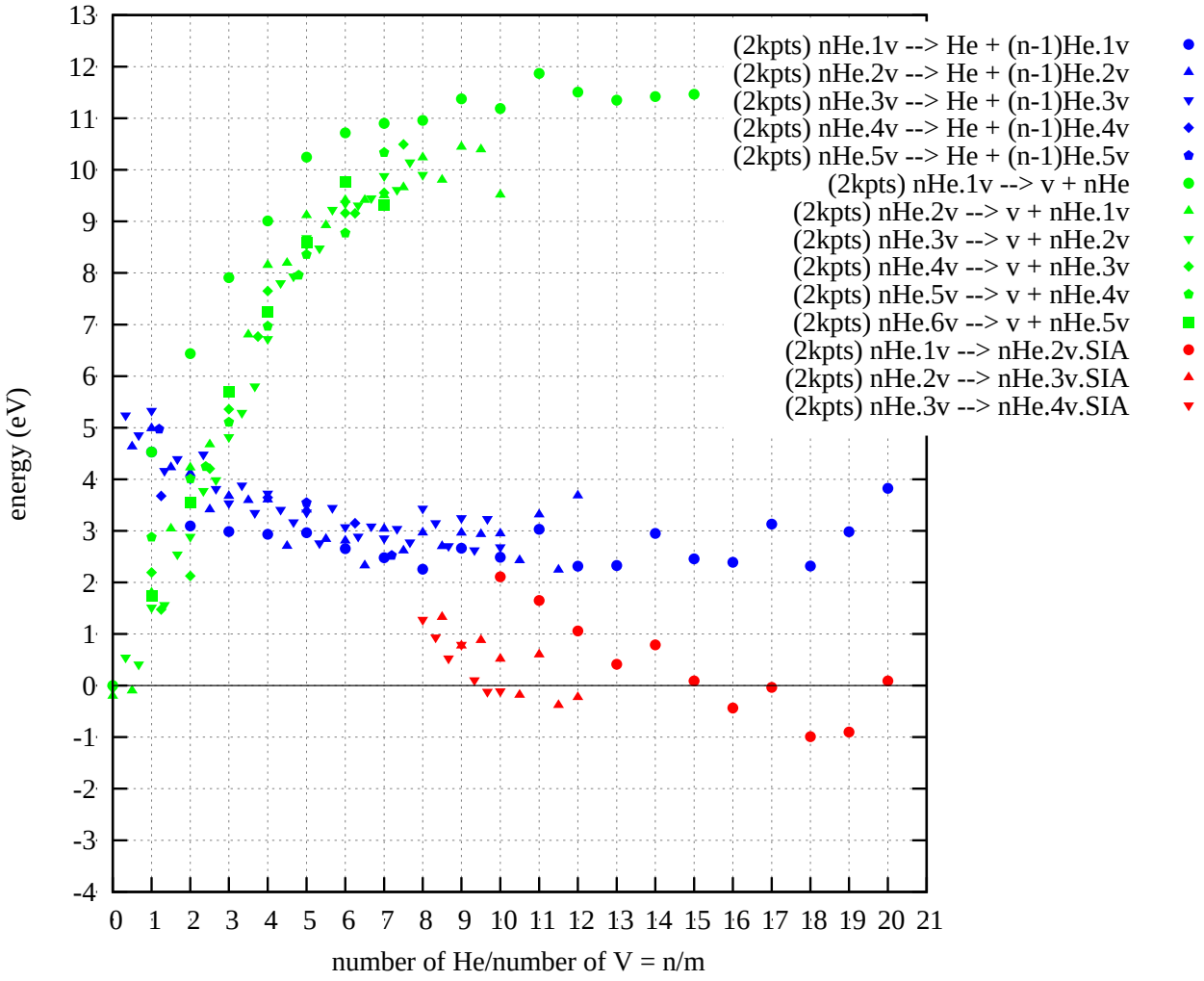

Figure 13: Stability of *n*He-*m*V clusters versus vacancy emission, helium emission and trap mutation as a function of n/m. Green symbols: vacancy binding energy (eV), blue symbols: He binding energy (eV), red symbols: energy to trap mutation (eV).

The fact that He atoms form bound complexes with vacancies in tungsten, prevent recombination between vacancies and SIAs generated by irradiation, and trap SIA defects, was confirmed by experiments by Hoffman et al. (2015). Experimental observations show that the implantation of helium into tungsten gives rise to lattice expansion that cannot be explained using ab initio data on relaxation volumes of vacancy or vacancy-helium defects. It is necessary to assume that SIA defects are retained in the helium-implanted layer. SIA defects have significantly larger relaxation volumes, and their presence can account for the observed swelling [Hofmann et al. (2015)]. The retention of SIAs and SIA clusters is caused by their attractive interaction with He-vacancy clusters, in agreement with atomistic simulations by Sandoval et al. (2015).

4.2.4 Mixed-interstitial transport:

Transmutant diffusion may also occur by way of interstitial defect-assisted transport. DFT calculations of the stability and mobility of Re and Os in W, with special focus on W-Re and W-Os mixed dumbbells, reveal potentially long-range transport mechanisms on the basis of the energetics obtained [Suzudo et al. (2014); Gharaee and Erhart (2015)]. Figure 14 shows the

relative formation energy of various types interstitials. The most energetically-favored configurations of the mixed Re interstitial is the <111> dumbbell, which can migrate by diffusing along the <111> direction. These energies imply that the mixed dumbbell can effectively rotate so as to move along any one of the four possible <111> directions. Additionally, as shown in Table 1, the dissociation energies of the mixed interstitials are quite high, while the migration energies along the <111> direction are very low. The combination of easy rotation, low migration energy, and high binding energy of the solute to the mixed dumbbell results in an effective three-dimensional diffusion with the defect never losing its mixed nature [Suzudo et al. (2015)]. This results in long-range solute transport in addition to that mediated by vacancies. These conclusions are generally applicable to Os mixed interstitials as well, although not in the same pronounced manner as for Re.

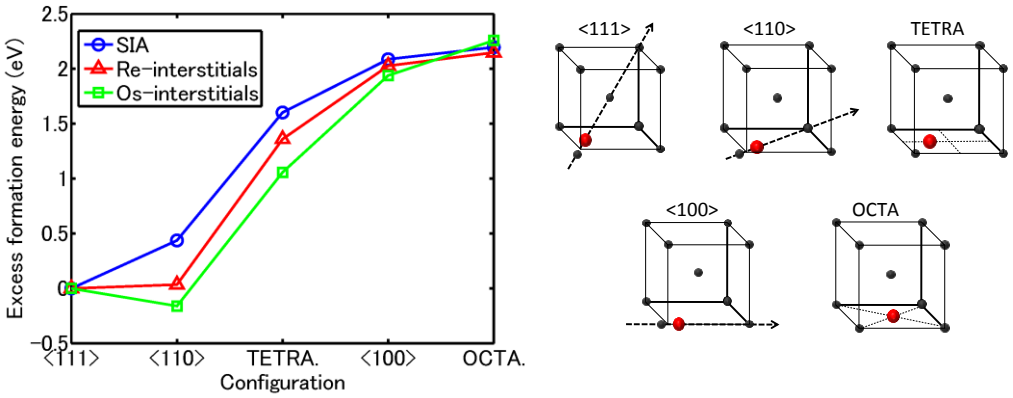

Figure 14: Relative formation energy of SIAs and Re and Os interstitials in W crystals.

Table 1 Dissociation energy of the most energetically favored mixed dumbbells into solute substitutional and SIA, and migration energy of W-Re and W-Os mixed dumbbells in W (eV):

Type of mixed dumbbell	Dissociation energy of mixed dumbbell	Migration energy of mixed dumbbell
W-Re	0.79	0.12
W-Os	1.87	0.31

4.3 PKA calculations

Another essential input to long-term damage accumulation calculations is the primary knock-on atom (PKA) spectrum. Fusion neutrons impinging on a material interact with its constituent atoms via a range of elastic, inelastic, and non-elastic (break-up) reactions, leading to an excited atom which may be displaced from its lattice site and, with sufficient energy, may initiate a sequence of displacement events known as a damage cascade. To completely predict the atomic recoils produced in a neutron-irradiated material, and hence to fully quantify the damage cascades, recoil events for all of the possible reactions channels in a material must be included. Using a recently developed computer code, SPECTRA-PKA [Gilbert, Marian, Sublet (2015)], which updates earlier work by Greenwood and Smither (1985) [see also Greenwood (1994)] to take advantage of more recent advances in computing and nuclear data technology, it is now a routine procedure to calculate the complete energy distributions of PKAs for any material in any neutron irradiation environment.

SPECTRA-PKA takes, as input, recoil energy versus incident-neutron energy probability (cross section) matrices for every nuclear reaction channel of every target nuclide in a composition,

which can be computed via the NJOY [MacFarlane et al. (2012)] nuclear data processing code. Figure 15a shows a 2D slice at a neutron energy of 14.1 MeV through the set of matrices computed by NJOY for the ^{184}W isotope (30.64 atomic % of natural W) from the TENDL-2014 [Koning et al. (2014)] data. There are many open reaction channels at this neutron energy, including an exothermic (n,α) (neutron capture followed by ^{4}He nucleus emission) reaction, explaining why the energy of the emitted light α-particle can be higher than the incident neutron energy (the blue vertical line in the plot). This complex picture then translates to large number of PKA distributions for ^{184}W when the matrices are merged by SPECTRA-PKA with the same typical DEMO first wall neutron spectrum used for the transmutation calculations described earlier. Figure 15b shows the resulting distributions for ^{184}W, but note that these have actually been simplified by summing together reaction channels that produce the same recoiling daughter (e.g. the pure elastic scattering and all inelastic scattering levels – only one of which was shown in Figure 15a – have ^{184}W as the recoiling species).

Of course, in a real material, the picture is even more complex because there will be many target nuclides. Figure 15c shows the complete set of PKA distributions under DEMO first wall conditions, summed as a function of element, for pure W, which has five naturally occurring isotopes. The elemental sums simplify the results greatly, but for reference note that distributions for more than 350 separate reaction channels were summed to create Figure 15c. The result shows that for W, the recoils from transmutant elements such as Ta and Hf are not significant compared to the dominant recoils of W atoms themselves. However, it is important to realize that this picture, in Figure 15c, is a t=0 snapshot of the recoils in a completely pure W under irradiation. In particular, it does not consider the situation after a period of irradiation where a significant proportion of transmutation products will have been created, particularly Re and Os (see the earlier section on transmutation), which would have their own sets of recoil distributions. The implication this has on the relative importance of recoils from different elements in W has been investigated elsewhere [Gilbert et al. (2016)], showing that a sizeable fraction of the total PKA rate comes from non-W recoils after a few years of irradiation.

As far as materials modeling is concerned, considering the information contained in Figure 15c, i.e. considering an evolving PKA spectrum as a function of the transmutation history, is still too complex for most purposes: in MD simulations of damage cascades (see below), typically only one element is considered for both the host lattice and the PKAs. Therefore, SPECTRA-PKA takes such results and performs additional simplifications to create both total distributions, where all heavy (light gas particles should be treated separately because the damage they create is very different) recoils are included, and then cumulative distributions, which can be used as sampling distributions in modeling simulations of radiation damage creation and evolution (see later). Figure 15d, shows the cumulative distribution function of recoils at t=0 in W and three other fusion relevant materials, under DEMO FW conditions. This result shows that in W, as expected, the PKAs are, on average, of lower energy than in lighter metals such as Fe – the average PKA energies (considering only energies above 10 eV) in W and Fe for the distributions in Figure 15d are, respectively, 4.4 and 20.9 keV.

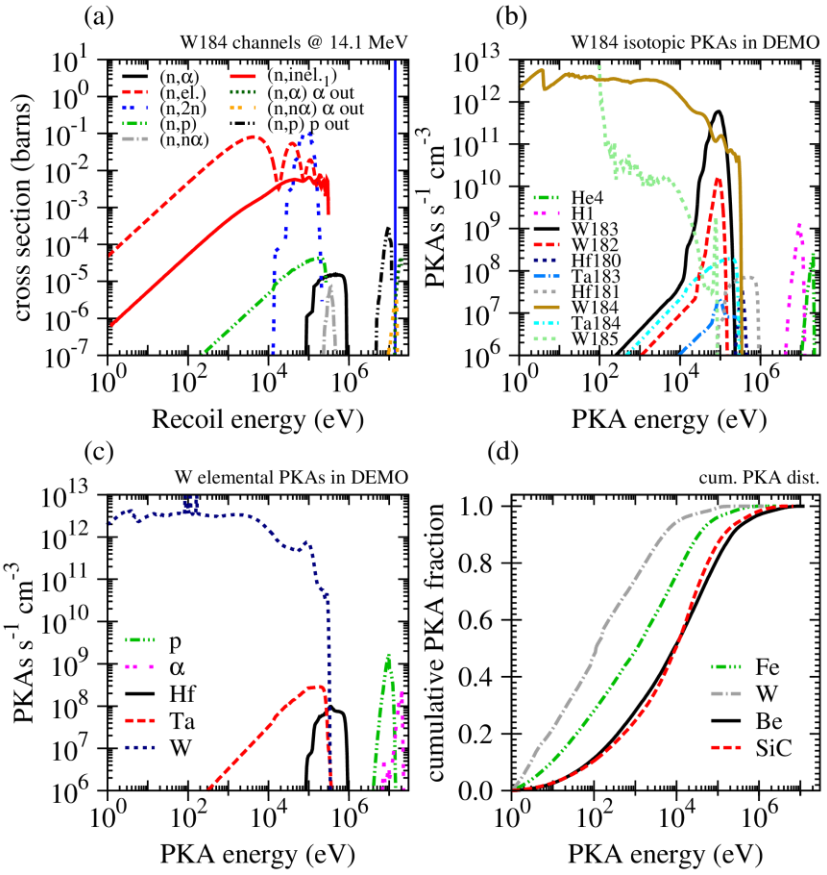

Figure 15: (color online) Computation of primary knock-on atom (PKA) distributions. (a) an example snap-shot showing the recoil probability cross sections for various reaction channels due to a 14.1 MeV (the blue vertical line in the plot) neutron impinging on ^{184}W. (b) the PKA rates produced for different isotopes when the energy dependent recoil cross sections for ^{184}W are collapsed (merged) with a typical first wall (FW) DEMOnstration fusion power plant. (c) the PKA rates summed as a function of element for pure W under DEMO FW conditions. (d) cumulative PKA distributions (summed over non-gas recoil elements) for Fe, W, Be, and SiC under DEMO FW conditions. Standard isotopic compositions, densities, and molar masses were used where necessary.

4.4 MD simulations of cascade damage

The next logical step is to translate PKA energies into defect numbers and size distributions. This connection is made by resorting to atomistic methods capable of simulating 10^5~10^7 atoms (depending on PKA energy), where a lattice atom is assigned an energy consistent with the pertinent PKA spectrum (e.g. as calculated above) along a specific lattice direction, and the system is evolved in time as the PKA deposits its energy throughout the lattice in what is known as a displacement cascade. The method of choice for conducting these simulations is again MD using semiempirical potentials. This is a mature procedure, dating back to the 1960s with the first simulation of a collision cascade in a model Cu system [Gibson et al. (1960)]. During the 1990s extensive MD studies of collision cascades were conducted by several groups [Ghaly and Averback (1994); Foreman et al. (1994); Gades and Urbassek (1995); Diaz de la Rubia (1996); Stoller et al (1997); Bacon et al (1997); Spacz'er et al. (1997); Nordlund et al. (1998)], all of which have had a profound impact in the way we understand irradiation damage in materials. The reader is referred to the relevant literature for discussions on the physical analysis of displacement cascades and their effect on the theory of irradiation damage (for a comprehensive review, see Averback et al. (1997)).

Simulations of cascade damage in tungsten are found to give good agreement with field ion microscopy experiments of ion irradiated W [Zhong et al (1998)]. However, while defect numbers predicted by different interatomic potentials are in general agreement [Fikar et al (2007)], the spatial distribution of interstitial defects shows sensitivity to the choice of potential [Fikar et al (2009)]. Another molecular dynamics study of collision cascades in nanocrystalline W found that grain boundaries inhibit the recombination of defects during recrystallization of the heat spike, leading to a higher number of surviving SIAs as compared to single-crystal simulations [Park et al (2009)]. More recently, MD modeling of high-energy cascades has been revisited by two groups using advanced interatomic potentials. A collaboration between researchers at the University of Helsinki in Finland and CCFE in the UK resulted in a validated semi-fractal model for high energy cascades in thin films [Sand et al. (2013); Yi et al. (2015)]. Simulations showed that a high degree of branching of recoil trajectories leads to a compact cascade core, resulting in the relatively frequent in-cascade formation of large defect clusters. Such defect clusters are formed in the strongly disordered core region, which spans roughly 25 nm, as illustrated in Fig. 16. The size-frequency distribution of clusters in the MD simulations was compared to self-ion irradiations with energies of 150 keV and a temperature of 30 K, where the size and spatial distributions were extracted by digitalizing and analyzing the experimental micrographs. Figure 17 shows the size histogram of cascade defects and its comparison with the irradiation experiments. The r.h.s. of the figure shows the extraction of defect sizes as a function of position from TEM micrographs. Among other interesting features of the cascade simulations, it was shown that defects generated in the simulations cannot be treated as isolated, as the positions of dislocation loops are correlated as demonstrated by the existence of significant elastic forces between the loops.

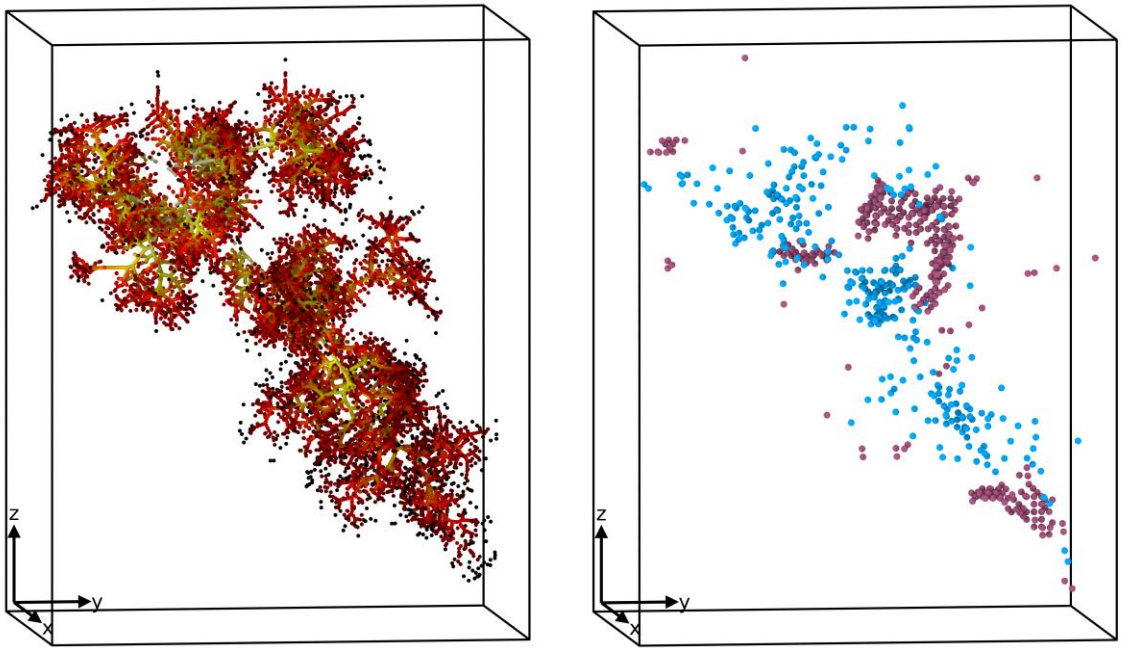

Figure 16: (Left) Recoils with E_{kin} > 10 eV in a collision cascade in W from a 200 keV PKA, colored according to the time from the initial PKA impact, ranging from 0 fs to about 300 fs, when recoils with such energies cease to exist. (Right) Final Wigner-Seitz defects from the same cascade, after 40 ps simulation time. Vacancies are represented by blue spheres and interstitials by red spheres. The dimensions (x,y,z) of the surrounding box are (15,20,25) nm.

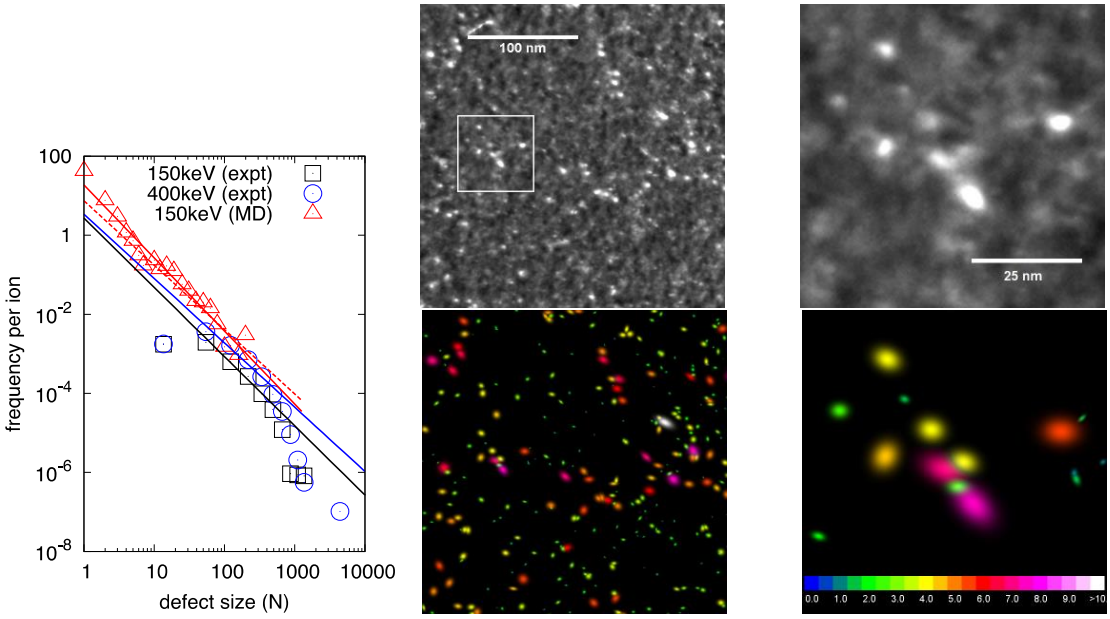

Figure 17: (Left) Histogram of defect size (N) for both experiments and MD simulations. The smallest size experimental bin is the accumulated frequency for diameter d < 1.5nm. The dashed line shows the defect cluster size power law found for 150 keV cascades in bulk tungsten [Sand et al (2013)]. The experimental histograms are normalized so that the area under the curves matches the total number of defects counted. (Right) Computational interpretation of the position and size of the defects in the TEM images above. Defects are colored according to their maximum diameter, with the scale (in nm) given in the colored bar. Figures are from [Yi et al (2015)].

Independently from these results, groups at PNNL and UT-Knoxville have conducted a large number of MD simulations to characterize cascade damage in tungsten caused by neutrons [Setyawan et al. (2015a); Setyawan et al. (2015b)]. PKA energies ranging from 100 eV to 200 keV initiated cascades at 300, 1025, and 2050 K. It was seen that the number of surviving Frenkel pairs (N_F) depended strongly on PKA or cascade damage energy (E_{MD}), but only a weak temperature dependence was observed. Two distinct damage regimes were found within this energy range. The two regimes intersect at a transition energy, in which its temperature-dependent value falls within a narrow range of reduced cascade damage energy, μ, defined as E_{MD} divided by the threshold displacement energy for tungsten. The N_F data were fit to an equation of the form: $N_F = a(\mu)^b$, where *a* and *b* are constants. When μ is < ~250 the functional dependence of N_F on μ is sub-linear, and for μ > ~250 super-linear behavior is found, which corresponds to formation of very large SIA defect clusters and dislocation loops. Values for the fitted constants for each temperature and damage regime are given in Table 2. In addition, defect clustering was found to be asymmetric, with SIA clustering increasing with temperature, while vacancy clustering showed the opposite trend. Furthermore, SIA clustering increased with μ, but vacancy clustering was relatively independent of μ.

Table 2. Fitted power-law constants for cascade damage in tungsten [Setyawan et al. (2015a)]

T (K)	μ < μ*		μ > μ*		μ*
	a	*b*	*a*	*B*	
300	0.49	0.74	0.02	1.30	276
1025	0.39	0.74	0.01	1.36	237
2050	0.38	0.73	0.01	1.36	229

Power laws such as the ones extracted from Figure 17 and Table 2, are what is needed to define the damage source term in longer-term damage accumulation calculations, which will be described below. These power laws represent simple correlations from which to extract cascade defect numbers and their size after sampling PKA energies from PKA spectra. However, as anticipated earlier, cascade defects are spatially correlated after MD simulation timescales. This may mean that the true number of defects observed after MD simulations may decrease even further when allowed to evolve longer in time. For this, 'cascade ageing' simulations are performed using methods that respect the spatial distribution of defect but that are efficient enough to extend the timescales to meaningful values. Again, KMC suggests itself as the ideal tool to accomplish such a task. This is the subject of the next section.

4.5 KMC simulations

4.5.1 Cascade ageing

Nandipati et al. (2015a; 2015b) have developed an advanced lattice-based object kinetic Monte Carlo code called *KSOME* (kinetic simulation of microstructure evolution) to study microstructural evolution in materials under irradiation. *KSOME* was designed to treat the migration, emission, creation, transformation and interaction (reaction) of all types of intrinsic point defects and their complexes in crystalline materials. The interaction of these point defects with sinks such as dislocations, grain boundaries, and free surfaces are included along with events such as loop-punching or trap mutation. Transformation events can include rotation or change of direction of 1D-diffusing SIA clusters, or a vacancy loop transforming into a spherical void, or transformation of a glissile to a sessile dislocation loop. All the input data, including reaction events, is supplied to the simulation via text-based input files, allowing the user to define any type of system without modification of the code.

KSOME was used to study the effects of temperature and cascade damage energy on cascade annealing in tungsten [Nandipati et al. (2015a; 2015b)]. Annealing simulations of individual displacement cascades from 10 to 100 keV were performed using the cascade database described above. Annealing for 10 ns was done at the same temperature as the cascade. Figure 18 shows a plot of the temperature dependence of annealing efficiency (expressed as a fraction of the initial number of SIAs, N_0) for 75 keV PKAs. Annealing behavior is characterized by early recombination of vacancies and SIAs, which occurs in the first ~2 ns, followed by gradual escape of fast diffusing SIAs from the cascade damage zone. The greatest contribution to annealing efficiency is from the migration of very small SIA clusters, which migrate in 3D at elevated temperatures because they are able to easily change direction. Larger SIA clusters (> 5) migrate 1D because it is difficult for them to change direction. Because of their migration characteristics large SIA clusters have a much higher probability of not recombining with vacancies and escaping the cascade damage zone. Surprisingly, annealing efficiency shows an inverse U-shape temperature dependence with the greatest annealing occurring at 1025 K. Single cascade annealing behavior in tungsten is predominantly controlled by point defect spatial and cluster size distributions, and the relative mobility of interstitial versus vacancy clusters. Differences in the temperature dependence of cascade-induced defect clustering combined with defect migration behaviors are responsible for the inverse U-shape annealing efficiency temperature dependence.

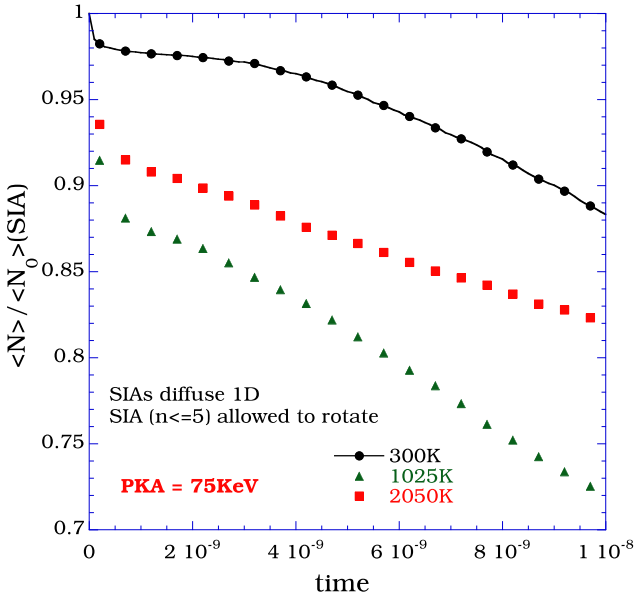

Figure 18: Temperature dependence of cascade annealing efficiency for 75 keV PKAs (average PKA for fusion neutron spectrum). Time is in seconds.

Defect production correlations to be used in damage accumulation models can then be updated with these aged defect distributions.

4.5.2 Simulations of SIA loop accumulation and interactions in thin films

Another useful feature of KMC calculations is that it can account for elastic effects due to long-range interactions between SIA loops. In a metal, elasticity is the predominant long-range interaction, and is the accepted driving force for dislocation mobility. The elastic energy between dislocation loops scales with the product of their areas and inversely with the cube of the separation between their centers, so two loops in W of 2 nm diameter and separated by 4 nm have an elastic interaction energy of order 1.0 eV [Mason et al. (2014)]. Elastic energy is therefore sufficient to bias microstructural evolution even for the smallest observable defects. This interaction is naturally captured in MD simulations, but in order to establish its impact on longer-term defect kinetics, it must be implemented in continuum kinetic codes such as object kinetic Monte Carlo or rate theory calculations. OKMC is well-suited to incorporating long-range elastic interactions because the spatial location of defects can be tracked with high accuracy. Mason et al. (2014) have shown that experimental observations of irradiated UHP W foil at elevated temperatures (to 800°C) were reproduced by a simple OKMC model accounting for elastic interactions. They demonstrated that the largest loops shrink at low temperatures, and the smallest glide away at high temperatures, accounting for both the observed reduction in total loop count and the changing distribution of loop sizes (Figure 19).

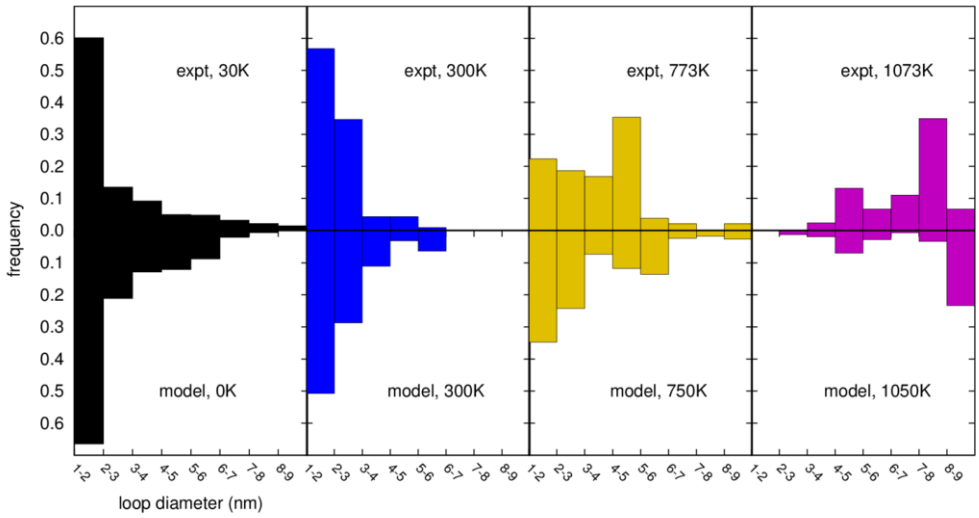

Figure 19: Histogram of sizes of defects observed after 150-keV W+ in W irradiation using *in situ* TEM, compared to object kinetic Monte Carlo modelling at 1 s after cascade initiation. After Mason et al. (2014).

As shown, kinetic Monte Carlo methods can provide valuable insights into what mechanisms operate at the atomic scale are carried over into longer time scales. However, in terms of damage accumulation, even the most efficient Monte Carlo codes fall short of providing meaningful irradiation doses (>0.1 dpa). Despite recent attempts at parallelization of kMC [Martinez et al. (2011); Jimenez and Ortiz (2016)], homogeneized rate theory methods based on the mean-field approximation may still offer the best potential in terms of reaching fusion-relevant irradiation doses (~10 to 100 dpa). In the next section, we present recent attempts at formulating mean-field models for fusion irradiation of W.

4.6 Mean field damage accumulation calculations

The last step in the multiscale sequence that we have followed throughout the paper is to evolve accumulated defect populations into diffusive timescales, on the order of 0.1 to 10 dpa. Next we introduce the stochastic cluster dynamics method (SCD) [Marian and Bulatov (2011)], which is a variant of the mean-field rate theory technique, alternative to the standard ODE-based implementations, that eliminates the need to solve exceedingly large sets of ODEs and relies instead on sparse stochastic sampling from the underlying kinetic master equation. Rather than dealing with continuously varying defect concentrations in an infinite volume, SCD evolves an integer-valued defect population N_i in a finite material volume Ω, thus avoiding combinatorial explosion in the number of ODEs. This makes SCD ideal to treat problems where the dimensionality of the cluster size space is high, e.g., when multispecies simulations—for example involving energetic particles, He, H, etc., simultaneously—are of interest. SCD recasts the standard ODE system into stochastic equations of the form:

$$\frac{dN_i}{dt} = \tilde{g}_i - \sum_j \tilde{s}_{ij} N_i + \sum_j \tilde{s}_{ji} N_j - \sum_{i,j} \tilde{k}_{ij} N_i N_j + \sum_{j,k} \tilde{k}_{jk} N_j N_k$$

where the set $\{\tilde{g}, \tilde{s}, \tilde{k}\}$ represents the reaction rates of 0th (insertion), 1st (thermal dissociation, annihilation at sinks), and 2nd (binary reactions) order kinetic processes taking place inside Ω. In diffusion-controlled systems, as is the case for bulk neutron irradiation, one must ensure that the characteristic diffusion length of any defect species is contained within the simulation volume at any given time, i.e. $\Omega^{1/3} > \square$, where $\square = \max\{l_i\}$ is the maximum diffusion length of any species i, and:

$$l_i = \sqrt{\frac{D_i}{R_i}}$$

Here, D_i and R_i are the diffusivity and the lifetime of a mobile cluster within Ω, with $R_i = \tilde{s}_i - \sum_j \tilde{k}_{ij} N_j$. To maintain a reasonable computational cost, the volume Ω is typically set at around 1 μm^3. The term $\tilde{g}$ is parameterized using PKA distributions such as those shown in Section 2.1.3, which in turn are translated into defect populations using cascade statistics from MD simulations (cf. Section 2.14). The coefficients $\tilde{s}$ represent defect annihilation at sinks and thermal dissociation, while $\tilde{k}$ represent chemical constants for binary defect reactions. Parameterization of these coefficients requires knowledge of diffusion activation energies, binding energies, and sink strengths for microstructural features including dislocations, grain boundaries, voids, and/or inclusions. Currently, a full parameter set for the energetics for transmutation products Re and Os is lacking in *ab initio* databases, and so our studies are limited to W-He systems, for which data – both from empirical interatomic potentials and from DFT calculations have been provided above.

An example of SCD simulations of damage accumulation in W under ITER conditions (equatorial plane of first wall), including transmutation He, is shown in Figures 20 and 21 [Marian and Hoang (2012)]. The associated size distributions of vacancy clusters (including vacancy-He bubbles) and interstitial clusters (dislocation loops) are shown in Figure.

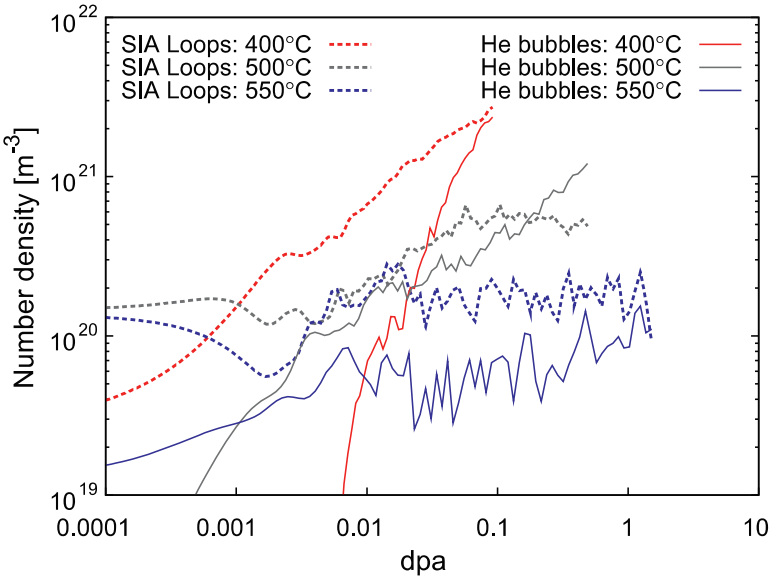

Figure 20. Accumulation of visible (>1.0 nm) SIA loops and He bubbles as a function of dose and temperature for the ITER irradiations.

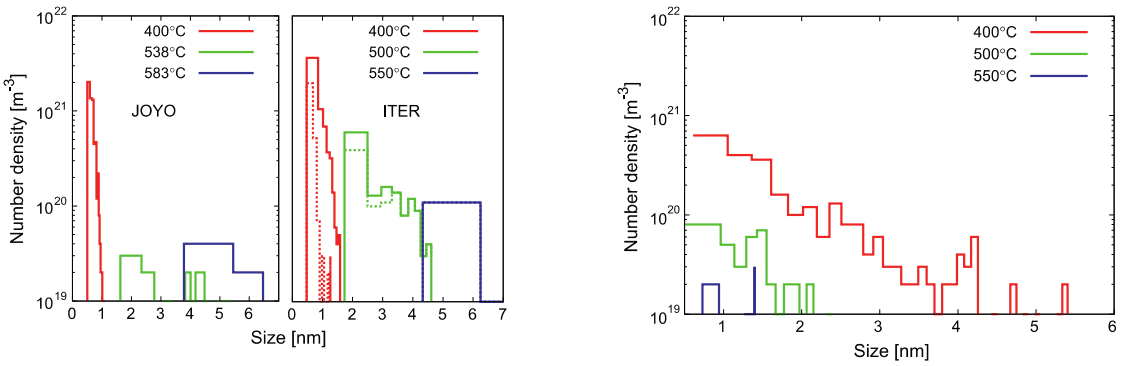

Figure 21. Size distributions of (left) vacancy clusters (including He bubbles, dashed lines) and SIA loops as a function of dose and temperature for ITER irradiations.

These distributions can be used to estimate the level of swelling and hardness, and so a macroscopic connection can be made with experimental data at the end of the multiscale sequence. He production by (n,α) reaction in W subjected to fusion neutrons is not significant, and so He bubbles may not play the critical role in the bulk that they play in PFCs. Future work aimed at including the effect of Re and Os in the simulations will likely be at the center of upcoming simulation development efforts.

4.7 Beyond the mean-field treatment of microstructural evolution.

One of the major drawbacks of the mean-field treatment of microstructural evolution is the fact that the procedure of spatial averaging involved in the derivation of mean-field equations (see e.g. [Brailsford and Bullough (1972); Dudarev (2000)]) neglects spatial correlations between defect positions and makes it virtually impossible to treat interaction between the defects. MFRT can provide defect densities that can then be linked to mechanical behavior by way of effective correlations as, e.g., in the manner presented in the previous section. However, this still presents a fundamental difficulty within the multiscale modeling framework, as the existence of spatial correlations and local oscillations in the populations of defects is known to control the onset of irradiation-induced plastic processes such as strain localization and other dislocation-mediated phenomena.

An example of the fact that interaction between radiation defects fundamentally influences microstructural evolution is illustrated by an electron microscope image of ion irradiated W annealed at 800ºC shown in Figure 22 [Ferroni et al. (2015)].

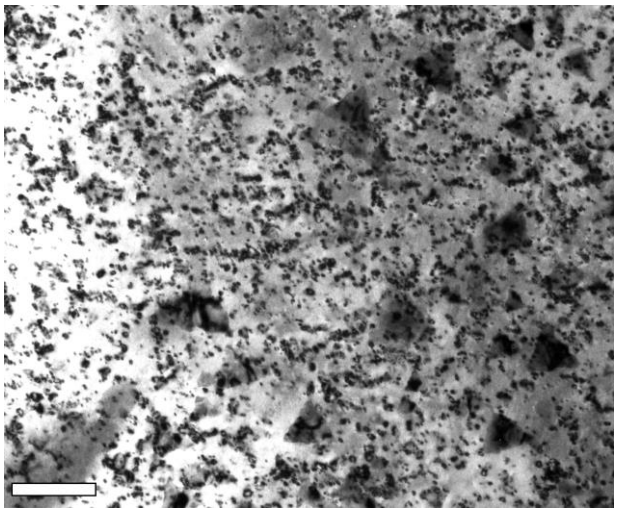

Figure 22: Electron microscope image of a high purity tungsten foil irradiated with 2 MeV W+ ions at 500°C to the fluence of 10^{14} ions cm^{-2} at dose rate of 2.7×10^{10} ions cm^{-2} s^{-1}, and subsequently annealed for 1 hour at 800°C [Ferroni et al. (2015)]. The scale bar in the image corresponds to 200 nm.

The image shows that nanoscale dislocation loops form rafts, and these rafts are the dominant feature of the observed microstructure. The dislocation raft structure seen in the image cannot be described in the mean-field approximation, since the spatial positions of the nanoscale dislocation loops forming the rafts are strongly correlated. Analysis shows that the formation of dislocation raft structures is driven by elastic interaction, which self-traps prismatic dislocation loops in the elastic fields of other loops [Dudarev et al. (2010)]. The dynamics of formation of rafts in real space can be modelled using Langevin equations for the nanodislocation loops, which describe, in real time, the stochastic Brownian motion of the loops biased by elastic interactions between them [Dudarev et al. (2014)]. The energy scale of elastic interactions varies from a fraction of an eV to several eV.

5 Summary and Future Efforts

In this paper, we have provided a review of the recent progress achieved in modeling W as a structural material in fusion environments. We have shown that multiscale modeling is an active and healthy field, with mature elements accompanied by new and undefined aspects to which additional efforts must continue to be devoted. We have noted the most important approaches of the multiscale modeling hierarchy, highlighting recent results and the connections among them. DFT calculations continue to be an essential piece of information, providing accurate estimates of crucial material and defect properties that form the foundation of higher-level models. MD simulations also continue to play a pivotal role in our modeling strategies, by providing mechanistic information involving hundreds of million to billions of atoms, and increasingly more realistic microstructures. For their part, KMC calculations are critical in maintaining atomistic resolution yet extending MD time scales into measurable regions. Finally, rate theory continuum methods continue to be the workhorse for radiation damage accumulation and plasma surface interaction calculations. Most importantly, examples of how each of these elements are now integrated and linked into a coherent multiscale modeling sequence are becoming more common, which synergistically magnifies the value of the calculations and simulations performed at each scale.

The progress experienced by modeling and simulation of fusion materials has been made possible by the confluence of several factors, including (i) the development of advanced algorithms to tackle several important bottlenecks in materials simulation; (ii) availability of computational resources to materials researchers, including massively-parallel computer time allocations and high performance computing; (iii) the concurrent effort of groups throughout the world with a high degree of coordination and information exchange; (iv) the recognition of the role played by modeling and simulation as a complement to experimental measurements and to fill the gap where experimental facilities are still lacking or where measurements are incomplete or inconclusive. In all, the progress displayed is encouraging and promising in terms of future developments. However, a number of bottlenecks still remain, which will have to be addressed if multiscale modeling is to continue to play the role of a useful companion to real data. Among the many challenges still facing computational modeling of materials in fusion environments (including W) are:

- Validation of models with relevant experimental data and assessments of the validity of model predictions for prescribed ITER/DEMO conditions.
- The timescale problem of (i) achieving realistic irradiation dose rates in atomistic simulations, and (ii) extending these dose rates to meaningul dpa levels (in fusion enviroenments) is one of the most important challenges facing multiscale modeling today.
- Incorporation of material impurities, and the true transmutation chemistry, with its associated solute effects including precipitations, segregation, trapping, etc.
- Establishing accurate correlations between the simulated microstructures and materials response in terms of mechanical behavior and property degradation.

Acknowledgments

JM acknowledges support from DOE's Early Career Research Program. The work of RJK was supported by the U.S. Department of Energy, Offices of Fusion Energy Sciences and Advanced Scientific Computing Research under Contract DE-AC06-76RLO-1830. TS is supported by JSPS KAKENHI Grant Number 24561044 and 15K06672 to conduct this work. BDW acknowledges funding support through the Scientific Discovery through Advanced Computing (SciDAC) program on Plasma Surface Interactions, funded by U. S. Department of Energy, Office of Science, Advanced Scientific Computing Research and Fusion Energy Sciences, as well as partially supported by DOE Office of Fusion Energy Sciences grant DOE-DE-SC0006661. The work of MRG, DRM, SLD, AS, and KN has been carried out within the framework of the EUROfusion Consortium and has received funding from the Euratom research and training programme 2014-2018 under grant agreement No 633053. MRG, DRM, and SLD also acknowledge funding from the RCUK Energy Programme under grant number EP/I501045. The views and opinions expressed herein do not necessarily reflect those of the European Commission.

References

Amino, T., Arakawa, K., Mori H. , Philosophical Magazine Letters 91 (2011) 86-96.

Averback, R. S. and T. Diaz de la Rubia, Solid State Physics 51 (1997) 281-402.

Bacon, D. J., Valder, A. F., Gao, F., J. Nucl. Mater., 251 (1997) 1-12

Baldwin, M. J , Doerner, R. P., Nucl. Fusion 48 (2008) 035001.

Baldwin, M. J., Doerner, R. P., Nishijima, D., Tokunaga, K., Ueda, Y., J. Nucl. Mater. 390–391 (2009) 886–890.

Balluffi, R.W., Journal of Nuclear Materials 69 & 70 (1978) 240-263.

Becquart C. S. and Domain, C., Journal of Nuclear Material 386-388 (2009) 109.

Becquart C. S. and Domain, C., Physical Review Letters 97 (2006) 196402.

Becquart C. S., Domain C., Nuclear Instruments and Methods in Physics Research B 255 (2007) 23.

Becquart C. S., Domain, C., Sarkar, U., DeBacker, A. and Hou, M., Journal of Nuclear Material 403 (2010) 75-88.

Becquart, C. S., Barthe, M.-F., DeBacker, A., Physica Scripta T145 (2011) 014048.

Björkas, C., Henriksson, K. O. E., Probst, M., and Nordlund, K., J. Phys.: Condens. Matter 22 (2010) 352206.

Boisse, J, Domain, C, Becquart, C S, Journal of Nuclear Material 455 (2014) 10.

Boisse, J., DeBacker, A., Domain, C., Becquart, C. S., Journal of Material Research 29 (2014) 2374.

Bolt, H., Barabash, V., Federici, G., Linke, J., Loarte, A., Roth, J., Sato, K., Journal of Nuclear Materials 307–311 (2002) 43-52.

Brailsford, A. D., and Bullough, R., J. Nucl. Mater. 44 (1972) 121-135.

Cui, J., M. Li, J. Wang, Q. Hou, Nuclear Instruments and Methods B 352 (2015) 104-106.

Cusentino, M. A., K. D. Hammond, F. Sefta, N. Juslin, B. D. Wirth, Journal of Nuclear Materials 463 (2015) 347-350.

Dalla Torre, J., J. Bocquet, N. V. Doan, E. Adam, and A. Barbu, Phil. Mag. A 85 (2005) 549.

De Backer, A., Lhuillier, P.-E., Becquart, C. S. and Barthe M.-F., Journal of Nuclear Material 429 (2012) 78.

DEMO: http://fusionforenergy.europa.eu/

Derlet, P. M., Nguyen-Manh, D., & Dudarev, S. L., Physical Review B 76 (2007) 054107.

Diaz de la Rubia, T., Nucl. Instr. Meth. Phys. Res. B 120 (1996) 19.

Dudarev, S. L., Arakawa, K., Yi, X., Yao, Z., Jenkins, M. L., Gilbert, M. R., Journal of Nuclear Materials 455 (2014).

Dudarev, S. L., Gilbert, M. R., Arakawa, K., Mori, H., Yao, Z., Jenkins, M. L., et al. (2010). Langevin model for real-time Brownian dynamics of interacting nanodefects in irradiated metals. Physical Review B, 81, 224107.

Dudarev, S. L., Physical Review B 62 (2000) 9325.

Ezumi, N., Ohno, N., Uesugi, Y., Park, J., Watanabe, S., Cohen, S. A., Krasheninnikov, S. I., Pigarov, Y. A., Takagi, M., Takamura, S., Proceedings of the 24th European Physical Society Conference on Controlled Fusion and Plasma Physics, Berchtesgaden (1997, Max Plank Institute für Plasma Physik: Garching) Vol. 21A, p 1225.

Fang, L. W., X. Shu, and G.-H. Lu, J. Mater. Res. 30 (2015).

Federici, G., C. H. Skinner, J.N. Brooks, J. P. Coad, C. Grisolia, A. A. Haasz, A. Hassanein, V. Philipps, C.S. Pitcher, J. Roth, and W. R. Wampler and D.G. Whyte, Nuclear Fusion 41 (2001).

Fernandez, N., Ferro, Y. and Kato, D. Acta Materialia 94 (2015) 307.

Ferroni, F., Yi, X., Arakawa, K., Fitzgerald, S. P., Edmondson, P. D., & Roberts, S. G., Acta Materialia 90 (2015) 380-393.

Fichthorn, K. A. and W. H. Weinberg, J. Chem. Phys 95 (1991) 1090.

Fikar, J., Schäublin, R., J. Nucl. Mater. 386-388 (2009) 97-101.

Fikar, J., Schäublin, R., Nucl. Instr. and Meth. B, 255 (2007) 27-31.

Foreman, A. J. E., W. J. Phythian, and C. A. English, Rad. Eff. & Def. in Sol. 129 (1994) 25.

Gades, H. and H. M. Urbassek, Phys. Rev. B 51 (1995) 14559.

Gerasimenko, V.I., Mikhaĭlovskiĭ, I.M., Neklyudov, I.M., Parkhomenko, A.A., Velikodnaya, O.A., Tech. Phys. 43 (1998) 803-8..

Ghaly, M. and R. S. Averback, Phys. Rev. Lett. 72 (1994) 364.

Gharaee, L. and P. Erhart, J. Nucl. Mater. 467 (2015) 448.

Giannozzi, P., S. Baroni, N. Bonini, M. Calandra, R. Car, C. Cavazzoni, D. Ceresoli, G. L. Chiarotti, M. Cococcioni, I. Dabo, A. Dal Corso, S. Fabris, G. Fratesi, S. de Gironcoli, R. Gebauer, U. Gerstmann, C. Gougoussis, A. Kokalj, M. Lazzeri, L. Martin-Samos, N. Marzari, F. Mauri, R. Mazzarello, S. Paolini, A. Pasquarello, L. Paulatto, C. Sbraccia, S. Scandolo, G. Sclauzero, A. P. Seitsonen, A. Smogunov, P. Umari, R. M. Wentzcovitch, J. Phys.: Condens. Matter. 21 (2009) 395502.

Gibson, J. B., A. N. Goland, M. Milgram, G. H. Vineyard, Dynamics of radiation damage, Phys. Rev. 120 (1960) 1229.

Gilbert , M. R., Dudarev, S. L., Derlet, P. M., & Pettifor, D. G., Journal of Physics: Condensed Matter 20 (2008) 345214.

Gilbert, M. R. J.-Ch. Sublet, and R.A. Forrest, Tech. Rep., Handbook of activation, transmutation, and radiation damage properties of the elements simulated using FISPACT-II & TENDL-2014; Magnetic Fusion Plants, vol. 15, CCFE-R, 2015, 26, CCFE. (http://www.ccfe.ac.uk/fispact handbooks.aspx)

Gilbert, M.R., and J.-Ch. Sublet, Nuclear Materials and Energy (2016) article in press.

Gilbert, M.R., Dudarev, S.L., Zheng, S., Packer, L.W., Sublet, J.-Ch., Nucl. Fus. 52 (2012) 083019.

Gilbert, M.R., J. Marian, and J.-Ch. Sublet, Journal of Nuclear Materials 467 (2015) 121.

Gilbert, M.R., L.W. Packer, J.-Ch. Sublet, and R.A. Forrest, Nucl. Sci. Eng. 177 (2014) 291.

Greenwood, L.R., J. Nucl. Mater. 216 (1994) 29-44.

Greenwood, L.R., Smither, R.K., Specter: Neutron Damage Calculations for Materials Irradiation, January 1985 document Number: ANL/FPP/TM-197. SPECTER and SPECOMP are available from: the NEA databank, http://www.oecd-nea.org/tools/abstract/detail/psr-0263.

Hammond, K. D. , F. Ferroni and B. D. Wirth, submitted to Fusion Science & Technology (2016)

Hammond, K. D. and B. D. Wirth, Journal of Applied Physics 116 (2014) 143301.

Hasegawa, A., M. Fukuda, T. Tanno and S. Nogami, Mater. Trans. 54 (2013) 466-471.

Hasegawa, A., T. Tanno, S. Nogami, M. Satou. J. Nucl. Mater. 417 (2011) 491-494.

Heinola, K., T. Ahlgren, K. Nordlund, and J. Keinonen, Phys. Rev B 82 (2010) 094102.

Henkelman, G., B. P. Uberuaga, and H. Jónsson, Journal of Chemical Physics 113 (2000) 9901.

Henriksson, K. O. E., K. Nordlund, and J. Keinonen, Nucl. Instr. Meth. Phys. Res. B. 244 (2006) 377.

Hill, K. W., Bitter, M., Eames, D., von Goeler, S., Goldman, M., Sauthoff, N. R., Silver, E., Low Energy X-Ray Emission from Magnetic Fusion Plasmas, Princeton University Technical Report PPPL–1807 (2000) (Princeton University, Princeton, New Jersey).

Hirooka, Y., Conn, R. W., Sketchley, T., Leung, W. K., Chevalier, G., Doerner, R., Elverum, J., Goebel, D. M., Gunner, G., Khandagle, M., Labombard, B., Lehmer, R., Luong, P., Ra, Y., Schmitz, L., Tynan, G., J. Vac. Sci. Technol. A. 8 (1990) 1790–1797.

Hofmann, F., Nguyen-Manh, D., Gilbert, M. R., Beck, C. E., Eliason, J. K., Maznev, A. A., Liu, W., Armstrong, D.E.J., Nelson, K.A., and Dudarev S.L., Acta Materialia 89 (2015) 352-363.

Hu, L. , K. D. Hammond, B. D. Wirth, and D. Maroudas, Journal of Applied Physics 115 (2014) 173512

Ito et al., J. Nucl. Mater. 463 (2015) 109.

Ito, A.M. , Y. Yoshimoto, S. Saito, A. Takayama, and H. Nakamura, Phys. Scr. T159 (2014) 014062.

Iwakiri, H, Yasunaga, K, Morishita, K, Yoshida, N., J. Nucl. Mater. 283–287 (2000) 1134–1138.

Jiménez, J., and Ortiz, C. J., Computational Materials Science 113 (2016) 178-186.

Juslin, N. and Wirth, B. D., Journal of Nuclear Material 432 (2013) 61.

Kajita, S., Sakaguchi, W., Ohno, N., Yoshida, N., Saeki ,T., Nucl. Fusion 49 (2009) 095005.

Kajita, S., Takamura, S., Ohno, N., Nishijima, D., Iwakiri, H., Yoshida, N., Nucl. Fusion 47 (2007) 1358–1366.

Kästner, J. and P. Sherwood, Journal of Chemical Physics 128 (2008) 014106.

Kato, D., Iwakiri, H., Watanabe, Y., Morishita, K. and Muroga, T, Nuclear Fusion 55 (2015)

Koning, A.J., D. Rochman, S.C. van der Marck, J. Kopecky, J.-Ch. Sublet, S. Pomp, H. Sjostrand, R.A. Forrest, E. Bauge, H. Henriksson, O. Cabellos, S. Goriely, J. Leppanen, H. Leeb, A. Plompen, R. Mills, S. Hilaire, TENDL-2014, Available from: ftp://ftp.nrg.eu/pub/www/talys/tendl2014/tendl2014.html (Release Date: December 11, 2014.).

Kornelsen E. V., Radiation Effects 13 (1972) 227.

Krasheninnikov, S. I., Phys. Scr. T145 (2011) 014040.

Kresse, G. and J. Hafner, Physical Review B 47 (1993) 558.

Lasa, A., et al., Nucl. Instrum. Meth. Phys. Res. B 303 (2013) 156.

Lasa, A., S. K. Tahtinen and K. Nordlund, EPL 105 (2014) 25002.

Leppanen, H. Leeb, A. Plompen, R. Mills, S. Hilaire, TENDL-2014, Available from: ftp://ftp.nrg.eu/pub/www/talys/tendl2014/tendl2014.html (Release Date: December 11, 2014.).

Li, H., Wurster, S., Motz, C., Romaner, L., Ambrosch-Draxl, C. and Pippan, R. Acta Materialia 60 (2012) 748.

Li, M. et al., J. Nucl. Mater. 433 (2013) 17.

Liu Y.L., Zhang Y., Zhou H.B., Lu G.H., Liu F. and Luo G.N. Physical Review B 79 (2009) 172103.

Liu, Y.-L., Zhou, H.-B., Zhang, Y., Lu, G.-H., Luo, G.-N., Computational Materials Science 50 (2011) 3213-3217.

Lu, G.-H., Zhou, H.-B. & Becquart, C.S., Nuclear Fusion 54 (2014) 086001.

MacFarlane, R.E., D.W. Muir, R.M. Boicourt, and A.C. Kahler, The NJOY Nuclear data processing system e LA-UR-12-27079 (http://t2.lanl.gov/nis/publications/NJOY2012.pdf).

Marian, J. and Bulatov, V. V., J. Nucl. Mater. 415 (2011) 84.

Marian, J. and T. L. Hoang, Journal of Nuclear Materials 429 (2012) 293-297

Maroudas, D. , S. Blondel, L. Hu, S. Blondel, K.D. Hammond, and B.D. Wirth, "Helium segregation on surfaces of plasma-exposed tungsten", Journal of Physics: Condensed Matter 28 (2016) 064004.

Martin-Bragado, I., Abujas, J., Galindo, P.L. and Pizarro, J., Nuclear Instruments and Methods in Physics Research B 352 (2015) 27.

Martin-Bragado, I., Rivera, A., Valles, G., Gomez-Selles, J.-L. and Caturla, M.-J, Computer Physics Communications 184 (2013) 2703.

Martinez, E., J. Marian, M. H. Kalos, and J. M. Perlado, Journal of Computational Physics 227 (2008) 3804-3823.

Martynenko and Nagel, Plasma Physics Reports 38 (2012) 996.

Mason, D.R., Yi, X., Kirk, M.A., and Dudarev, S.L., J. Phys.: Condens. Matter 26 (2014) 375701.

Matolich, J., Nahm H., Moteff, J., Scipta Metallurgica 8 (1974) 837-842

Miyamoto, M., D. Nishijima, M.J. Baldwin, R.P. Doerner, Y. Ueda, K. Yasunaga, N. Yoshida, and K. Ono, Journal of Nuclear Materials 415 (2011) S657-S660.

Muzyk, M., Nguyen-Manh, D., Kurzydłowski, K. J., Baluc, N. L., & Dudarev, S. L., Physical Review B 84 (2011) 104115.

Nandipati, G. Setyawan, W., Heinisch, H.L., Roche, K.J., Kurtz, R.J., Wirth, B.D., Journal of Nuclear Materials 462 (2015a) 338.

Nandipati, G., Setyawan, W., Heinisch, H.L., Roche, K.J., Kurtz, R.J., Wirth, B.D., Journal of Nuclear Materials 462 (2015b) 345.

Nemoto Y., Hasegawa A., Satou M. Abe K., J. Nucl. Mater. 283-287 (2000) 1144-1147.

Nguyen-Manh, D and Dudarev S. L., Nuclear Instruments and Methods in Physics Research B 352 (2015) 86.

Nguyen-Manh, D., Horsfield, A. P., & Dudarev, S. L., Physical Review B 73 (2006) 020101.

Nishijima D, Ye M-Y, Ohno N, Takamura S 2004 J. Nucl. Mater. 329–333 1029–1033.

Nishijima, D., Miyamoto, M., Iwakiri, H., Ye, M.-Y., Ohno, N., Tokunaga, K., Yoshida, N., Takamura, S., Mater. Trans. 46 (2005) 561–564.

Noda, T., Fujita, M., Okada, M., J. Nucl. Mater. 258-263 (1998) 934-939.

Nordlund, K., M. Ghaly, R. S. Averback, M. Caturla, T. Diaz de la Rubia, J. Tarus, Phys. Rev. B 57 (1998) 7556.

Ohsawa, K. Goto, J. Yamakami, M., Yamaguchi, M. and Yagi, M. Physical Review B 82 (2010) 184117.

Opplestrup, T., V. V. Bulatov, G. H. Gilmer, M. H. Kalos, and B. Sadigh, Phys. Rev. Lett. 97 (2006) 230602.

Pan, B. C. and Wang, Z.-G., AIP Advances 3 (2013) 012118.

Park, N.-Y., Cha, P.-R., Kim, Y.-C., Seok, H.-K., Han, S.-H., Lee, S.-C., Cho, S., Jung, H., Met. Mater. Int., 15 (2009) 447-452.

Pentecoste, L., Brault, P., Thomann, A.-L., Desgardin, P., Lecas T., Belhabib, T., Barthe, M.-F. and Sauvage, T, Journal of Nuclear Materials, 470 (2016) 44.

Pereslavtsev, P., L. Lu, U. Fischer, and O. Bitz, Fus. Eng. Des., 89 (2014) 1979.

Perez, D., T. Vogel and B.P. Uberuaga, Physical Review B 90 (2014) 014102.

Qin, S.-Y., Jin, S., Sun, L., Zhou, H.-B, Lu, G.-H. Journal of nuclear materials 465 (2015) 135.

Raffray, A.R., R. Nygren, D.G. Whyte, S. Abdel-Khalik, R. Doerner, F. Escourbiac, T. Evans, R.J. Goldston, D.T. Hoelzer, S. Konishi, P. Lorenzetto, M. Merola, R. Neu, P. Norajitra, R.A. Pitts, M. Rieth,M. Roedig, T. Rognlien, S. Suzuki, M.S. Tillack, and C. Wong, Fusion Engineering and Design 85 (2010) 93.

Ruzic, D. N., and H. K. Chiu, Journal of Nuclear Materials 162–164 (1989) 904.

Ruzic, D. N., Nuclear Instruments and Methods B 47 (1990) 118.

Sand, A. E., S. L. Dudarev and K. Nordlund, EPL 103 (2013) 46003.

Sandoval, L., Perez, D., Uberuaga, B. P., & Voter, A. F., Pysical Review Letters (2015) 105502.

Sefta, F., K. D. Hammond, N. Juslin and B. D. Wirth, Nuclear Fusion 53 (2013) 073015.

Sefta, F., N. Juslin and B.D. Wirth, Journal of Applied Physics 113 (2013) 243518

Setyawan, W., Nandipati, G., Roche, K.J., Heinisch, H.L., Kurtz, R.J., Wirth, B/D., Journal of Nuclear Materials, 462 (2015a) 329.

Setyawan, W., Nandipati, G., Roche, K.J., Kurtz, R.J., Wirth, B.D., Fusion Materials Semiannual Progress Report for the Period Ending June 30, 2015, DOE/ER-0313/58 (2015b) 272.

Sharafat, S., Takahashi, A., Nagasawa, K., Ghoniem, N., J. Nucl. Mater. 389 (2009) 203–212.

Smirnov, R. D., S.I. Krasheninnikov and J. Guterl, Journal of Nuclear Materials 463 (2015) 359-362.

Snead, L. L., D. T. Hoelzer, M. Rieth, A. Nemith, "Refractory Alloys, Vanadium, Niobium, Molybdenum, Tungsten." In: Structural Materials for Nuclear Energy Applications. Elsevier. Edited by S. J. Zinkle. and G. R. Odette. To be published.

Snead, L. L., L M Garrison, T S Byun, N A P K Kumar, W D Lewis. "Evaluation of Mechanical Properties of Tungsten after Neutron Irradiation. Fusion Reactor Materials Program December 31, 2013 DOE/ER-0313/55-Vol 55 pg 40-47.

Snead, L. L., to be published in Journal of Nuclear Materials (2016).

Soler, J. M. , E. Artacho,J. D. Gale, A. García, J. Junquera, P. Ordejón, and D. Sánchez-Portal, J. Phys.: Condens. Matt. 14 (2002) 2745-2779.

Spacz'er, M., A. Almazouzi, R. Schäublin, and M. Victoria, Rad. Eff. & Def. in Sol. 141 (1997) 349.

Stoller, R. E., Odette, G. R., Wirth, B. D., J. Nucl. Mater. 251 (1997) 49-60.

Stoller, R. E., S. I. Golubov, C. Domain, and C. S. Becquart, Journal of Nuclear Materials 382 (2008) 77-90.

Sublet, J.-Ch., J.W. Eastwood, J.G. Morgan, M. Fleming, and M. R. Gilbert, The FISPACT-II User Manual, Tech. Rep. CCFE-R(11)11 Issue 7 (2015). (http://www.ccfe.ac.uk/fispact.aspx)

Suzudo, T., Yamaguchi, M., and Hasegawa, A., Journal of Nuclear Materials 467 (2015) 418.

Suzudo, T., Yamaguchi, M., and Hasegawa, A., Modelling and Simulation in Materials Science and Engineering 22 (2014) 075006.

Takamura, S., Ohno, N., Nishijima, D., Kajita, S., Plasma Fusion Res. 1 (2006) 051.

Tanno, T., A. Hasegawa, J. C. He, M Fujiwara, M Satou, S Nogami, K Abe, T. Shishido, Journal of Nuclear Materials 386-388 (2009) 218-221.

Terentyev, D., Dubinko, V., Bakaev, A., Zayachuk, Y., Van Renterghem, W. and Grigorev, P. Nuclear Fusion 54 (2014) 042004.

Thompson, M.W., The damage and recovery of neutron irradiated tungsten, Philosophical Magazine, 5:51 (1960) 278-296.

Umstadter, K. R., Doerner, R., Tynan, G., Phys. Scr. T138 (2009) 014047.

Valles, G., González, C., Martin-Bragado, I., Iglesias, R., Perlado, J.M., Rivera, A., Journal of Nuclear Materials 457 (2015) 80

Van der Kolk, G. J., van Veen, A., de Hosson, J. Th. M. and Caspers, L. M., Nuclear Instruments and Methods in Physics Research B 6 (1985) 517.

Vanderbilt, D., Phys. Rev. B **41** (1990) 7892.

Ventelon, L., Willaime, F., Fu, C.-C., Heran, M., and Ginoux I., Journal of Nuclear Materials 425 (2012) 16.

Voter, A. F., F. Montalenti, and T. C. Germann, Annu. Rev. Mater. Res. 32 (2002) 321.

Voter, A. F., Introduction to the Kinetic Monte Carlo Method. In: Sickafus KE, Kotomin EA, editors. Radiation Effects in Solids. Dordrecht, The Netherlands: Springer (2005). NATO Publishing Unit.

Voter, A.F., Phys. Rev. B 57 (1998) R13985.

Wirth, B. D. , K. Nordlund, D. G. Whyte, and D. Xu, Fusion materials modeling: challenges and opportunities, MRS Bulletin 36 (2011) 216.

Wirth, B. D., K. D.. Hammond, S. I. Krashenninikov, and D. Maroudas, Journal of Nuclear Materials 463 (2015) 30-38.

Wright G M, Brunner D, Baldwin M J, Doerner R P, Labombard B, Lipschultz B, Terry J L, Whyte D G 2012 Nucl. Fusion 52 042003.

Xiao, W. and Geng, W.T. Journal of Nuclear Materials 430 (2012) 132.

Xolotl: https://sourceforge.net/projects/xolotl-psi/

Yi, X., A. E. Sand, D. R. Mason, M. A. Kirk, S. G. Roberts, K. Nordlund, S. L. Dudarev, EPL 110 (2015) 36001.

You, Y.W., Kong, X.S., Wu, X.B., Xu, Y.C., Fang, Q.F., Chen, J.L., Luo, G.-N., Liu, C. S.,

Zenobia, S. J., Kulcinski, G. L., Phys. Scr. T138 (2009) 014049.

Zhong, Y., Nordlund, K., Ghaly, M., Averback, R. S., Phys. Rev. B 58 (1998) 2361-2364.

Zhou H.-B, Liu, Y.-L., Jin, S., Zhan, Y. Luo, G.-N. and Lu, G.-H. Lu, Nuclear Fusion 50 (2010) 025016.

Zhou, H-B., Liu, Y-L., Zhang, Y., Jin, S., Lu, G-H. Nuclear Instruments and Methods in Physics Research B 267 (2009) 3189.

Zhou, H. –B, Jin, S., Zhang, Y. and Lu, G. -H, Science China: Physics, Mechanics and Astronomy, 54 (2011) 2164.

Zhou, H.-B., Jin, S., Zhang, Y. and Lu, G.-H , Progress in Natural Science: Materials International 21 (2011) 240.

Ziegler, J. F., editor, The Stopping and Range of Ions in Solids, volume 1 of The Stopping and Ranges of Ions in Matter, Pergamon Press, New York, 1985.

Zinkle, S. J., and Busby, J. T., Materials Today 12 (2009) 12-19.

Zinkle, S. J., and Ghoniem, N. M., J. Nucl. Mater. 417 (2011) 2-8.